




**Pitch perturbation effects on a revolving wing at low Reynolds number**Shantanu S. Bhat <sup>1,\*</sup>, Soudeh Mazharmanesh,<sup>2</sup> Albert Medina,<sup>3</sup> Fang-Bao Tian,<sup>1</sup>  
John Young <sup>1</sup>, Joseph C. S. Lai <sup>1</sup> and Sridhar Ravi<sup>1</sup><sup>1</sup>*School of Engineering & IT, University of New South Wales, Canberra, ACT 2612, Australia*<sup>2</sup>*School of Civil Engineering, The University of Sydney, Sydney, NSW 2008, Australia*<sup>3</sup>*U.S. Air Force Research Laboratory, Wright-Patterson Air Force Base, Ohio 45433, USA*

(Received 1 March 2023; accepted 19 September 2023; published 12 October 2023)

Low-aspect-ratio revolving wings find applications in miniature robotic flyers and turbomachinery. At a high angle of attack, the flow separates from a wing's leading edge, forming a leading-edge vortex. On a revolving wing, the leading-edge vortex (LEV) is stabilized by strong rotational acceleration and is known to be the primary source of high and stable aerodynamic forces acting on the wing. While previous studies have characterized the performance of revolving wings, the effects of perturbations on the flow profile and performance have not been explored. This study combined experiments and computational fluid dynamics simulations to investigate the lift, drag, and power coefficients of a wing revolving at a Reynolds number of  $Re = 2500$  and undergoing pitch perturbations. Perturbations were systematically varied to investigate the effects of the wing's initial angle, the amplitude and duration of perturbation, and the location of the pitch axis. Simulations provided insights into the flow structures around the wing and their effects on the wing-surface pressures and the aerodynamic forces. Finally, a quasisteady model was used to decompose the effects of wing rotation and pitch perturbations on the lift and drag forces. The decomposition revealed a consistent dependency of the variations in the lift on the pitch angular velocity across all perturbations, irrespective of the initial angle. The transition from the LEV-dominant to the rotation-dominant flow occurs at very low pitch rates, the values of which were found to depend on the initial angle of the revolving wing. For lower initial angles, the transition occurred at lower pitch rates. During the rotation-dominant perturbations, changes in the vortical structures around the wing were found to have a minimal effect on the lift and drag compared to the quasisteady effects. Moreover, the oscillations in the lift and drag during the perturbation could be reduced by appropriately shifting the pitch axis location. These findings highlight the dominant role of inviscid effects on the variations in loads acting on a revolving wing during pitch perturbations.

DOI: [10.1103/PhysRevFluids.8.104701](https://doi.org/10.1103/PhysRevFluids.8.104701)**I. INTRODUCTION**

Fluid dynamics of revolving wings are of high interest to engineers for their applications in turbomachines, rotorcrafts, and microair vehicles. The geometry of a revolving wing can be broadly defined by the ratio of the wingspan ( $b$ ) to the mean wing chord ( $\bar{c}$ ), also known as the aspect ratio ( $AR = b/\bar{c}$ ). In the context of revolving wings, the Rossby number is also an important parameter, defined as  $Ro = R_g/\bar{c}$ , where  $R_g$  is the wing's radius of gyration. The kinematics of the wing is characterized by its Reynolds number ( $Re = U_{ref}\bar{c}/\nu$ ), where  $U_{ref}$  is the reference velocity, typically

\*s.bhat@adfa.edu.au

at the radius of gyration of the wing, and  $\nu$  is the kinematic viscosity of the fluid around the wing. Motivated by the flight of winged seeds and insect wings at low Reynolds numbers ( $Re < 10^5$ ), the aerodynamics of small-aspect-ratio wings ( $AR < 5$ ) have been investigated for their possible small-size engineering applications [e.g., Refs. 1–3].

The flow over unperturbed low-Reynolds-number revolving wings is significantly different from that over translating wings, as has been revealed by several studies motivated by flapping wings of insect [e.g., Refs. 4–7]. In this Reynolds numbers regime, at a high angle of attack, the flow over a revolving wing separates at its leading edge, forming a leading-edge vortex (LEV) over the wing's suction surface [5]. Due to the spanwise gradient of the flow during the wing's rotation (sweep motion), the LEV also varies in size along the span, causing it to be smaller near the wing root and larger towards the wing tip. For a wing held at a constant angle ( $\alpha$ ) and rotating with a constant angular velocity ( $\dot{\phi}$ ), the LEV is stabilized in its place and size throughout the wing's rotation. Such a rotational motion of the wing with constant  $\alpha$  and  $\dot{\phi}$  has also been called sweep, rotational translation or sometimes just translation in the literature [e.g., Refs. 8–10]. The mechanism behind the stability of the LEV has been investigated over several decades. The extra vorticity fed into the LEV of a revolving wing by the flow separated from its leading edge is carried away radially outward, contributing to the vorticity in the wake deposited from the wing tip [7]. Maxworthy [4] has attributed this to the spanwise pressure gradient over a revolving wing. However, more recent studies have attributed this to the action of strong centripetal and Coriolis accelerations [7,11]. Moreover, the vortex tilting has also been observed to be contributing to the stability of the LEV [12–14].

During rotational translation, the stably attached LEV creates a stable suction pressure on the wing surface beneath the LEV. Consequently, the forces on the revolving wing are also found to be stable [6,15]. However, a change in the wing's angle of attack due to the wing's rotation about its spanwise axis (pitch motion) may disturb the stability of the LEV, affecting the wing performance. Such disturbance may arise in the case, for example, of pitching-flapping perturbed revolving wings employed in microair vehicles [16] or during the pitch-oscillations in the flapping motion of wings [17]. However, the effects of such pitch perturbations on the flow and the forces on the wing remain under-explored. A systematic investigation of the effects of the kinematics of pitch perturbations on a revolving wing is necessary. Moreover, a deeper understanding of the factors responsible for the effects of pitch perturbations on wing performance is important so that the appropriate controls can be applied in robotic flyers with revolving wings undergoing pitch oscillations.

Many researchers in the past have explored the effects of pitch oscillations on linearly translating wings [e.g., Refs. 18–21]. In the absence of any oscillations, steady flow over such a wing exerts lift force on the wing, which increases with an increase in the wing's angle of attack until it reaches a stall angle. At or beyond the stall angle, the flow over the wing separates at its leading edge, causing a sudden drop in the lift. However, when a linearly translating wing is set to undergo pitch oscillations, the flow periodically reattaches and detaches from the wing surface, which causes the instantaneous lift values to differ from the static values at the same wing angles. These values' cycle undergoes a hysteresis during a pitching oscillation [22]. This phenomenon is commonly called dynamic stall [18]. Furthermore, at high angles of attack, the shear layer separated from the leading edge oscillates with a phase difference from the wing's pitch oscillations [23,24]. In such a case, the forces acting on the wing vary in magnitude depending on the strength and phase of the shear-layer oscillations. However, this does not explain the pitch-perturbation effects on revolving wings at low Reynolds numbers, which, unlike linearly translating wings, do not experience a static stall due to the stable attachment of the LEV. Hence, the possibility of a dynamic stall in revolving wings needs to be examined. It also remains unclear if prevailing quasisteady models developed for wings operating in quiescent conditions can predict wing performance during and after the perturbation. The use of such models will be highly beneficial for predicting the forces on perturbed revolving wings operating in realistic conditions.

In the past few years, Chen *et al.* [16,25] reported on the dynamic behavior of forces acting on a revolving wing at  $Re = 1500$  during its pitch and flapping perturbations. The initial angle of attack

of the wing ( $\alpha_0$ ) in these studies were  $0^\circ$  and  $20^\circ$  where the flow is nominally attached to the wing. The lift and drag on revolving wings depend highly on  $\alpha$  [8], and at higher angles of attack a stable LEV is formed [5,7]. Accordingly, the response of revolving wings to perturbations may also be different from that of linearly translating wings. More recently, Chen *et al.* [26] studied the pitch-up motion on a revolving wing and the associated vorticity dynamics for a fixed initial angle and perturbation amplitude. They showed that the LEV breaks up during sudden pitch-up manoeuvres while the vortex-tilting-based mechanisms are attenuated. Moving the pitch axis closer to the leading edge results in lift enhancement. However, the role of the relative velocity vector and the resulting local drag appears to be important here, which was not explored. Moreover, investigating wider ranges of  $\alpha_0$  and pitching amplitudes ( $\Delta\alpha$ ) is necessary to improve our understanding of the LEV and its dynamics applicable to a larger number of studies.

The present study focused on the effects of pitch perturbations on a revolving wing by systematically varying the initial pitch angle ( $\alpha_0$ ), the amplitude ( $\Delta\alpha$ ), the duration of perturbation ( $T_p$ ), and the combinations thereof. The effects of the pitch-axis location were also examined for a chosen case. This investigation required the measurement of forces and torques over the wing to analyze its performance and relate them to the surface pressure and flow field data to analyze the effects of the perturbation. The forces and torques were measured experimentally, for a wide parameter space. The surface pressure and flow-field data were evaluated for a subset of cases using computational fluid dynamics (CFD) simulations. Finally, the quasisteady model developed for flapping wings by Lee *et al.* [27] was explored for its applicability to pitch-perturbed revolving wings. The experimental and computational methods, and the quasisteady model are described in Sec. II. The forces acting on an unperturbed and perturbed wing are analyzed in Sec. III. The pressure and flow-field data from CFD are discussed in detail along with power-transfer calculations in Sec. IV, followed by the conclusions in Sec. V.

## II. METHODS

### A. Experimental method

Experiments were conducted on a rectangular wing of span  $b = 150$  mm and chord  $c = 50$  mm placed at the center of a water tank of size  $900 \times 900 \times 600$  mm<sup>3</sup>. This size was large enough to have minimal effects from sidewalls [28]. The schematic of the experimental setup is shown in Fig. 1(a). The wing was cut from a 1-mm-thick aluminium sheet and was provided with a root cutout of  $35 \times 21$  mm<sup>2</sup> to accommodate a force/torque sensor (ATI Nano17 IP68 F/T sensor) at its root, as shown in Fig. 1. The wing along with the sensor was attached to a timing pulley near the bottom of the main shaft of a flapping mechanism, driven by a timing belt and another pulley at the top. The motion of the main shaft about the sweep ( $Y$ ) axis and that of the timing pulley about the pitching ( $Z$ ) axis was provided by two identical RoboStar SBRS-5314HTG servo motors, as described by Ref. [29]. Due to the pulley and the attachments, the wing root was offset from the axis of rotation by  $b_0 = 20$  mm. The normalized offset  $b_0/b = 0.13$  was within the range of having a negligible effect on the LEV over the wing [30].

The wing was initially held at rest at a constant angle of attack  $\alpha_0$  and was then rotated about the  $Y$  axis with the Reynolds number of  $Re = \rho U_{\text{ref}} c / \mu = 2500$ , where the reference velocity is  $U_{\text{ref}} = 0.75R\dot{\phi}$ ,  $R$  is the wing-tip radius with respect to the sweep axis ( $R = b + b_0$ ),  $\dot{\phi}$  is the constant rotational velocity of the wing and  $\rho = 1000$  kg/m<sup>3</sup> and  $\mu = 8.9 \times 10^{-4}$  Pa·s are, respectively, the density and viscosity values of the water in the tank. In each experiment, the wing was rotated by 160 degrees in time  $T = 9$  s, involving the first 0.5 s of acceleration from rest, 8 s of constant rotation velocity  $\dot{\phi}$ , and the last 0.5 s of deceleration to rest. After the end of the motion, the wing was retracted to its initial position, followed by a rest period of 2 min to allow the disturbed water to settle back to its near-quiescent state. During the sweep motion at a constant  $\dot{\phi}$ , after time  $t_1 = 0.4T$ , the wing's angle of attack was increased by the amplitude  $\Delta\alpha$  using a constant pitch angular velocity until  $t_2 = t_1 + T_p/2$  and was returned to the original angle  $\alpha_0$  by  $t_3 = t_1 + T_p$ . Thus,  $T_p$  represents the

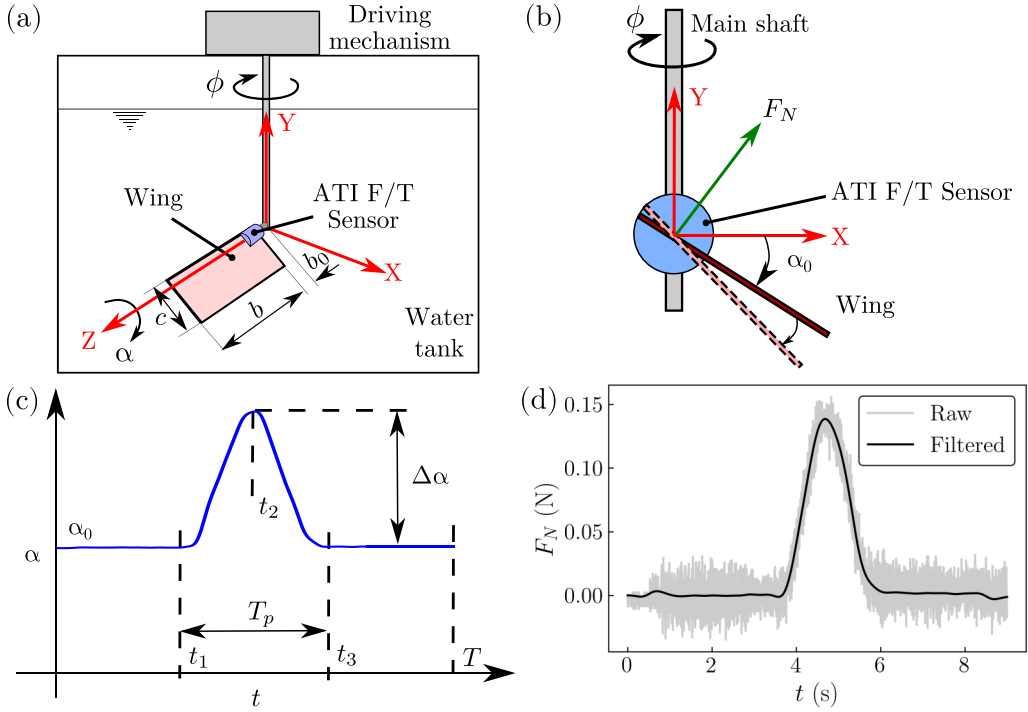


FIG. 1. The schematic shows (a) the rotating wing experimental setup in a water tank (not to scale), (b) the front view of the wing showing its initial angle  $\alpha_0$  and the magnitude of perturbation  $\Delta\alpha$ , and (c) recorded time traces of the wing angle  $\alpha$ , also showing the time period of the perturbation  $T_p$  and the time period of the rotational stroke  $T$ . A typical raw recorded signal for the normal force  $F_N$  and the same obtained after filtering it are shown in panel (d) for the case  $\alpha_0 = 15^\circ$ ,  $\Delta\alpha = 52^\circ$ , and  $\tau = 0.2$ .

total duration of the perturbation. The smooth variations in  $\alpha$  during the changes in pitch velocities can be approximated by the smoothing function given by OI *et al.* [21].

The forces and torques acting on the wing were measured by the ATI Nano17 IP68 F/T sensor at the sampling rate of 1000 Hz using a National Instruments PCI-6143 DAQ board linked to a PC. With the SI-50-0.5 calibration, the ATI sensor was capable of measuring forces in three dimensions with an accuracy of 12.5 mN and torques in three dimensions with an accuracy of 0.0625 mNm. Thus, the uncertainty in the force and torque measurements in the experiments were estimated to be  $\pm 6.25$  mN and  $\pm 0.0312$  mNm, respectively. The servo motors' potentiometer signals were recorded to estimate the wing's actual angular positions simultaneously with the force data. The total duration of an experiment included recording the forces and torques during the first 3 s of rest before the start, 9 s of wing rotation, and 3 s of rest after stopping the wing. Each experiment was repeated five times and the filtered lift and drag data were found to be highly repeatable within the margin of 3% for the largest pitch perturbation of the chosen parameter space.

The recorded raw data were processed using an in-house Python code. The raw data were filtered at the cutoff frequency of  $f_c = 4/T_p$  using a fourth-order Butterworth filter. A comparison of a raw recorded normal force  $F_N$  and the filtered force data can be seen in Fig. 1(d). The recorded forces were considered to be the sum of the translational, rotational, gravitational, inertial, and added-mass forces. Thus, to isolate the fluid-mechanical forces, it was necessary to subtract the remaining force components. The gravitational forces were obtained by recording the forces while the wing was held in water in its steady state. The inertial forces were obtained by repeating the experiments in air and subtracting the weight in the air, since the fluid-mechanical forces are negligible in air. For

analyzing the translational and rotational components of the fluid-mechanical forces, as discussed later in the results, the added-mass forces were subtracted from the measurements. The added-mass force and torque were estimated by the expressions given by [27]

$$F_{\text{am}} = f_a \rho \frac{\pi}{4} \left[ \ddot{\phi} \sin \alpha \int_0^R c(r)^2 r dr + \ddot{\alpha} \int_0^R c(r)^2 \left( \frac{c(r)}{2} - x_{\text{rot}} \right) dr \right] \quad \text{and}$$

$$\tau_{\text{am}} = -f_i \rho \frac{\pi}{128} \ddot{\alpha} \int_0^R c(r)^4 dr, \quad (1)$$

respectively, where  $f_a = 0.773 + 1.903\text{Re}^{-0.687}$  and  $f_i = 1.056 + 7.49\text{Re}^{-0.855}$  are the Reynolds-number correction factors,  $c(r)$  is the local chord length at a spanwise distance  $r$ ,  $x_{\text{rot}}$  is the chordwise distance of the pitch axis from the leading edge,  $\phi$  is the sweep-angular displacement, and  $\alpha$  is the pitch-angular displacement. The fluid-mechanical forces obtained after subtracting the gravitational, inertial, and added-mass components were used to compute the lift ( $L$ ) and drag ( $D$ ) forces acting along the  $Y$  and  $X$  directions, respectively, in the rotating frame of reference, as shown in Fig. 1(b). Here, the lift and drag coefficients are defined as

$$C_L = \frac{2L}{\rho U_{\text{ref}}^2 S} \quad \text{and} \quad C_D = \frac{2D}{\rho U_{\text{ref}}^2 S}, \quad (2)$$

respectively, where  $S$  is the wing area. The  $C_L$  and  $C_D$  throughout this work represent the coefficients of fluid-mechanical forces without the added mass component.

The initial angle  $\alpha_0$  and the perturbation amplitude  $\Delta\alpha$  were both systematically varied in the range  $[0^\circ-90^\circ]$  in the steps of  $15^\circ$ . Both pitch-up and pitch-down perturbations were investigated. Two different values of the normalized duration of perturbation  $\tau = T_p/T = 0.2$  and  $0.4$  were chosen. Note that the actual recorded values of  $\Delta\alpha$  with  $\tau = 0.2$  were found to be, approximately, in the multiples of  $13^\circ$  and those with  $\tau = 0.4$  were found to be, approximately, in the multiples of  $14.5^\circ$  due to the limitation of the motor's acceleration to quickly reach the target constant pitch speed.

## B. Numerical method

The numerical method used here has been adopted from that of Refs. [31,32], which has been validated for rotating and flapping wings in the range of the Reynolds numbers  $150 \leq \text{Re} \leq 4000$ . Flow over the wing was simulated by directly solving Navier-Stokes equations in a noninertial rotating frame of reference using the commercial code Ansys CFX 21.1.

In this method, a rectangular wing, offset from the rotation axis similar to that in experiments, was located at the center of a cylindrical domain of diameter  $18R$  and height  $48c$ , as shown by the schematic in Fig. 2(a). The rotation axis of the wing was aligned with the axis of the cylinder. The domain was split into the outer ‘‘rotary’’ subdomain and the inner ‘‘pitching’’ subdomain. The inner spherical pitching subdomain of diameter  $2.4R$  was situated at the center of the cylindrical domain. The entire domain was discretized using an unstructured tetrahedral mesh with triangular prism elements near the wing surface. Following the recommendations of Ref. [31], a time step of  $T/(2\phi_A)$  was used, where  $T$  is the total duration of the rotational stroke and  $\phi_A$  is the total rotation amplitude in degrees. Grid convergence was ensured by repeating the case with  $\alpha_0 = 15^\circ$ ,  $\Delta\alpha = 52^\circ$ , and  $\tau = 0.2$ , using coarse, medium, and fine grids obtained by changing the grid spacing by a factor of 2 in each refinement. The timetraces of  $C_L$  and  $C_D$  for the three grids are shown in Figs. 2(b) and 2(c), respectively. Both instantaneous and mean variations in  $C_L$  and  $C_D$  were observed to be within 3% between the medium and fine grids. Hence, the medium grid was chosen for all simulations in the study. The overall mesh consisted of approximately 8 million elements, with a grid spacing of  $0.0145c$  on the wing surface.

The top and bottom faces of the cylinder were modelled as Dirichlet boundaries, each held at zero gauge pressure. The cylindrical surface was modelled as a free-slip wall. The wing surfaces were

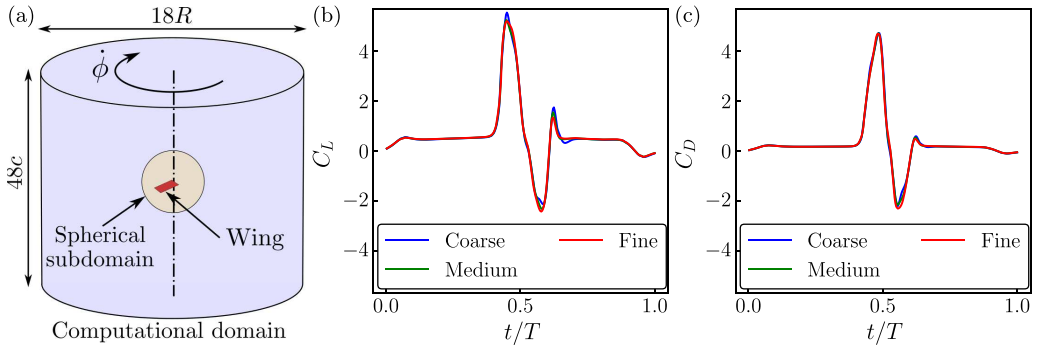


FIG. 2. The schematic of the computational domain is shown in panel (a). The time traces of (b)  $C_L$  and (c)  $C_D$  from coarse (minimum grid spacing,  $\Delta x = 0.0289c$ ), medium ( $\Delta x = 0.0145c$ ), and fine ( $\Delta x = 0.00725c$ ) grids are compared for the case with  $\alpha_0 = 15^\circ$ ,  $\Delta\alpha = 52^\circ$ , and  $\tau = 0.2$ .

modelled as no-slip walls. The mesh in the inner spherical subdomain was fixed with respect to the wing and was allowed to rotate about the wing's pitching axis with the angular velocity  $\dot{\alpha}$  using the ‘‘Mesh Motion’’ tool in Ansys CFX. A general grid interface (GGI) connection was applied at the interface between the two nonconformal subdomains.

The wing was initially set to be at rest at an angle  $\alpha_0$  with the horizontal plane. It was then accelerated within the first 0.5 s to the rotational velocity  $\dot{\phi} = 20$  deg/s and was then rotated with a constant rotational velocity until  $t = 8.5$  s, followed by a deceleration to  $\dot{\phi} = 0$  deg/s within the final 0.5 s. The pitch angle  $\alpha$  underwent one perturbation  $\Delta\alpha$  during this motion, the same as that described in the experimental method. As mentioned earlier, the actual variation in  $\alpha$  in experiments was observed to be different from the target profile. Hence, the variation in  $\alpha$  in the numerical simulations was specified using the cosh function with its smoothing coefficient and amplitude adjusted to closely match the experimental data of  $\alpha$ , as shown in Fig. 3(a).

Two cases were simulated for validating the numerical method; first, with  $\Delta\alpha = 13^\circ$ , and second, with  $\Delta\alpha = 52^\circ$ . In both cases,  $\alpha_0 = 15^\circ$  and  $\tau = 0.2$  were chosen to be the same. Figures 3(b) and 3(c) show the time traces of  $C_L$  and  $C_D$  predicted by CFD. For both cases, the time traces of  $C_L$  match the experimental data better than the time traces of  $C_D$ . The dimensional drag forces produced by the wing for  $\Delta\alpha = 13^\circ$  are very small, which fall within the range of uncertainty of our measurements. For the case of  $\Delta\alpha = 52^\circ$ , the mean  $C_D$  in experimental measurements are lower compared to CFD;

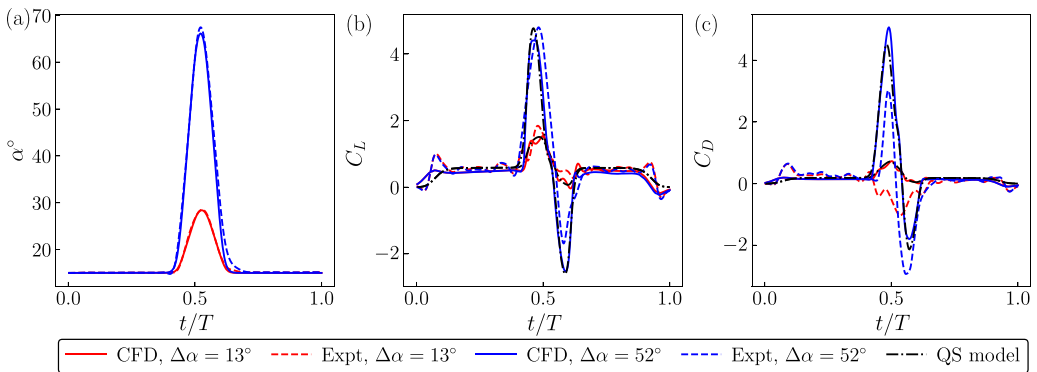


FIG. 3. Time traces of (a)  $\alpha$ , (b)  $C_L$ , and (c)  $C_D$  are shown for two different perturbation amplitudes,  $\Delta\alpha = 13^\circ$  and  $52^\circ$ . In both cases,  $\alpha_0 = 15^\circ$  and  $\tau = 0.2$ . The CFD predictions are compared with the experimental data and the quasisteady model predictions [27].

however, their peak-to-peak variations are similar. Overall, noting a higher discrepancy between the experiments and simulations in the mean  $C_D$  values, the results and discussions in this work rely primarily on the analysis of  $C_L$  values, which show a better match with CFD simulations.

### C. Quasisteady model

Several quasisteady (QS) models have been developed in the past [e.g., by Refs. 27,33–35], predicting the forces and torques on rotating and flapping wings. The QS model proposed by Lee *et al.* [27] takes into account the effects due to the wing’s Reynolds number, aspect ratio, and Rossby number, which are important parameters having coupled effects on the wing performance [36]. The QS model of Lee *et al.* [27] was derived for a 3D flapping wing under the assumption that the wing operates at sufficiently low Rossby numbers (Ro) at which “the LEV is highly stable and vortex shedding is prevented.” While the early development of the LEV is similar between 2D and 3D wings, its structure in the later stages is remarkably different [9,12]. The LEV on low-Ro 3D revolving wings is stabilized due to the action of the strong spanwise flow driven by the centripetal and Coriolis accelerations [7,11], typically absent in 2D wings. This assumption is also valid for the revolving wing in our study with  $Ro = 2.27$ . Thus, the applicability of a QS model has been explored to predict the forces on pitch-perturbed revolving wings in this study.

The model of Lee *et al.* [27] was employed here to evaluate the feasibility of simplified QS models to predict the transient force response to perturbations on the wing. Comparisons between experimental, simulation and model predictions would also provide insights into the force generation mechanism by decomposing the forces into various components. For the purpose of analyzing various force components and their dependence on the wing’s kinematic parameters, the relevant equations in the model of Lee *et al.* [27] are described in the Appendix for reference.

This model considers the instantaneous lift and drag acting on the wing as combinations of contributions from quasisteady effects due to the wing’s rotation about the span-normal axis (called the translational effects) and about the pitching axis (called the rotational effects) as well as the added mass effects. Moreover, the wing in this model is assumed to be rigid, flat, and thin. The rotational effects are assumed to result in the forces acting only in the wing-normal direction. Correction factors have been proposed by Lee *et al.* [27] to account for the changes in the results based on the wing’s Reynolds number, aspect ratio, and Rossby number, as described in the Appendix. Overall, it can be seen that the predictions of  $C_L$  and  $C_D$  from the QS model bear good similarity to the CFD predictions. The differences between the experimental data and QS model predictions observed for some cases are within the experimental uncertainty limits, similar to the differences between the experimental data and CFD predictions mentioned in Sec. II B. The decomposition of forces using the QS model was used to analyze various effects, as discussed in the results.

## III. RESULTS

### A. Unperturbed revolving wing

For a rotationally translating wing, the values of  $C_L$  and  $C_D$  are directly related to the angle of attack  $\alpha_0$ , which would remain constant throughout the rotation in the absence of any perturbations. Several previous studies have reported constant values of  $C_L$  and  $C_D$  with a constant  $\alpha_0$  during rotation [e.g., Refs. 6,37,38]. Studies, such as Refs. [6,39,40], have shown that the mean values of  $C_L$  and  $C_D$  vary similar to those shown in Fig. 4(b). As an example, timetraces of  $C_L$  and  $C_D$  for the case  $\alpha_0 = 60^\circ$  are shown in Fig. 4(a). During the initial acceleration from rest, both  $C_L$  and  $C_D$  experienced a sudden increase followed by a decrease until reaching a plateau. Even with such a high  $\alpha_0$ , both  $C_L$  and  $C_D$  could be seen to be nominally stable. Several studies in the past [e.g., Refs. 6,7,30,38,39] have shown that the LEV over a steadily rotating wing remains stably attached to the wing and is responsible for the stable aerodynamic forces experienced by the wing even at high angles. The oscillations in the values observed in Fig. 4(a) during this time are within

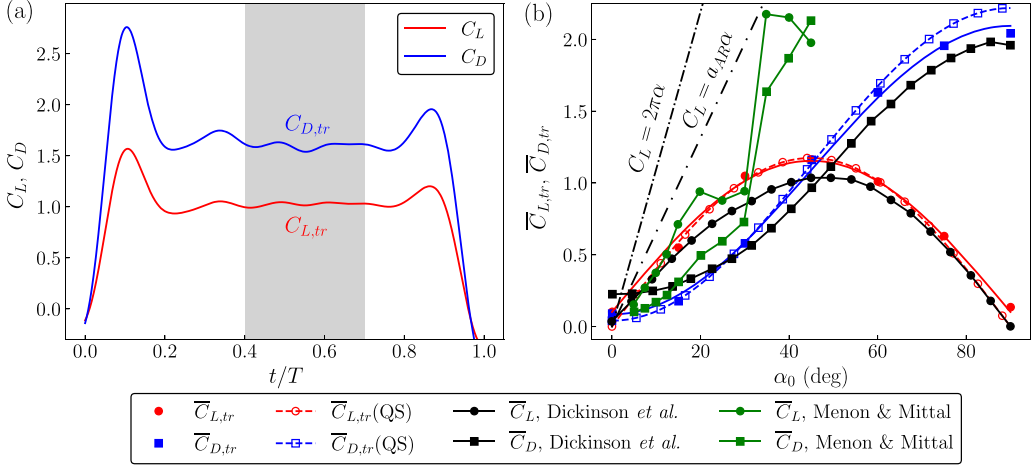


FIG. 4. The timetraces of  $C_L$  and  $C_D$  of the wing in pure rotation at  $\alpha_0 = 60^\circ$  are shown in panel (a). The mean steady values in the shaded region in panel (a), i.e.,  $\bar{C}_{L,tr}$  and  $\bar{C}_{D,tr}$  are shown as functions of  $\alpha_0$  in panel (b). Here, the red and blue continuous lines show the fits to  $(\sin 2\alpha_0)$  for the  $\bar{C}_{L,tr}$  data and to  $(1 - \cos 2\alpha_0)$  for the  $\bar{C}_{D,tr}$  data, respectively. The filled colored symbols represent the present data. The thin dashed lines with open symbols represent the predictions using the quasisteady model of Lee *et al.* [27]. The data for a revolving fruitfly wing at  $Re = 136$  by Dickinson *et al.* [6] and a translating NACA0015 airfoil at  $Re = 2000$  by Menon and Mittal [41] have been compared. The dash-dot lines show the  $C_L - \alpha$  relation for a translating wing of an infinite aspect ratio (slope  $2\pi$ ) and a finite aspect ratio (slope  $a_{AR}$ ).

the experimental uncertainties due to vibrations and noise. Unlike the linearly translating wings, revolving wings do not experience stall even at high angles.

The stabilized values of  $C_L$  and  $C_D$  were averaged over the period  $0.4 < t/T < 0.7$  to obtain their steady values  $\bar{C}_{L,tr}$  and  $\bar{C}_{D,tr}$ , respectively. By changing the wing angle  $\alpha_0$  in different sets of experiments, the values of  $\bar{C}_{L,tr}$  and  $\bar{C}_{D,tr}$  were obtained as functions of  $\alpha_0$ , as shown in Fig. 4(b). In the case of 2D wings, for example, Menon and Mittal [41] have shown that a linearly translating NACA0015 wing, characterized by  $Ro = \infty$ , at  $Re = 2000$  experiences mild stall at  $20^\circ \leq \alpha \leq 25^\circ$ , as can be seen in Fig. 4(b). At higher angles ( $\alpha \geq 35^\circ$ ), it experiences deep stall, apparent from the sudden drop in  $\bar{C}_L$ . However, the changes in  $C_{L,tr}$  with  $\alpha$  for revolving wings are gradual. Moreover, a 2D wing's performance can be seen to be significantly different from that of a 3D wing. As expected, the  $\bar{C}_{L,tr}$  data from experiments fit well to the  $(\sin 2\alpha_0)$  function and the  $\bar{C}_{D,tr}$  data fit well to the  $(1 - \cos 2\alpha_0)$  function, in line with the relation shown by the QS model [see Eq. (A5)]. These fits show a close match to the predictions of the QS model except at high angles, i.e.,  $\alpha_0 > 70^\circ$ , as can be seen in the figure. Moreover, there is an agreement between the experimental data of Dickinson *et al.* [6] and the present data. For the purpose of the comparison with common reference scales ( $U_{ref} = 0.75R\dot{\phi}$ ), the data of Dickinson *et al.* [6] was scaled by the factor  $R_g^2 / (0.75R)^2$ . The actual values might still differ due to the differences in their wing shape (*Drosophila* wing planform) and Reynolds number ( $Re = 136$ ). In this figure, a line representing the  $C_L = 2\pi\alpha$  function for a translating wing of an infinite aspect ratio has also been shown for reference. Moreover, a line for a translating finite-aspect-ratio wing has also been shown to match the current AR. The slope of this line is given by

$$a_{AR} = \frac{a_0}{1 + \frac{a_0}{\pi AR}}, \quad (3)$$

where  $a_0 = 2\pi$  is the slope of the line for an infinite aspect ratio. Overall, the  $C_L - \alpha$  relation for revolving (or rotationally translating) wings highly deviates from the  $C_L = 2\pi\alpha$  relation given by



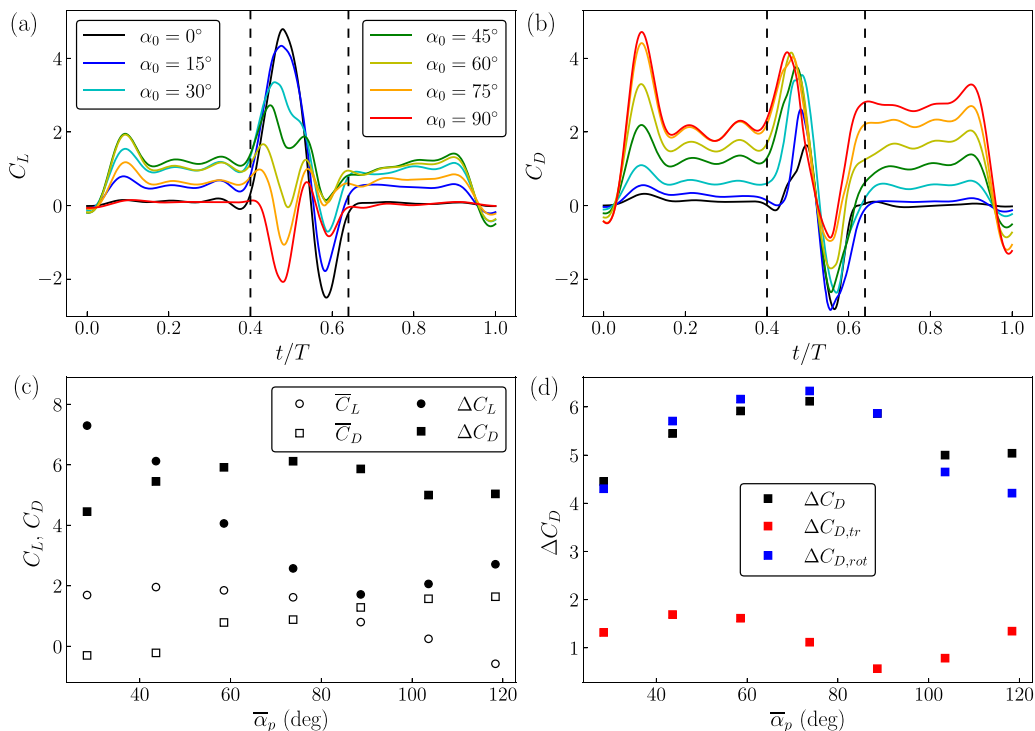


FIG. 5. Time traces of (a)  $C_L$  and (b)  $C_D$  are shown for various  $\alpha_0$ . Across all the cases compared here,  $\Delta\alpha = 52^\circ$  and  $\tau = 0.2$ . The start and end of perturbations are shown by dashed lines. The mean values  $\overline{C}_L$  and  $\overline{C}_D$ , and the peak-to-peak variations  $\Delta C_L$  and  $\Delta C_D$  during the pitch perturbation are shown as functions of the mean pitch perturbation angle  $\overline{\alpha}_p$  in panel (c). Using the QS model,  $\Delta C_D$  values are further decomposed into the variations in the contributions from the translational effects ( $\Delta C_{D,tr}$ ) and rotational effects ( $\Delta C_{D,rot}$ ) in panel (d).

the thin airfoil theory for linearly translating wings. Furthermore, these results are in line with the result from the previous studies [6,39,40] that a small-aspect-ratio wing revolving at low Reynolds numbers does not experience stall as a linearly translating wing does.

### B. Effect of initial angle on a perturbed wing

A pitch perturbation introduced during steady rotation changes the instantaneous  $\alpha$ , which would alter the  $C_L$  and  $C_D$  experienced. The effect of the initial angle of attack on the variation in  $C_L$  and  $C_D$  due to a perturbation was analyzed by keeping  $\Delta\alpha = 52^\circ$  and  $\tau = 0.2$  as constant, and varying  $\alpha_0$  in the steps of  $15^\circ$ . Note that  $\Delta\alpha = 52^\circ$  has been chosen as a representative case and similar results were observed with other values of  $\Delta\alpha$ . Figure 5 shows that both  $C_L$  and  $C_D$  were affected by  $\alpha_0$ . As expected, both  $C_L$  and  $C_D$  initially increased when the wing was accelerated from rest, and they reached nearly stable values close to  $t/T = 0.2$ . From this point until the start of the pitch perturbation, the wing was in the pure rotational translation where the  $C_L$  and  $C_D$  were nominally steady, similar to the unperturbed cases discussed earlier. The variations observed in both  $C_L$  and  $C_D$  are due to the noise in the measurements. Note that the variation of 0.5 in  $C_D$  corresponds to the actual force value of  $\sim 3.4$  mN, which is a very small value to be detected in the experimental measurements. Such variations are also seen in other notable experimental studies, for example, by Refs. [40,42]. The CFD results in Fig. 3 confirm that those variations do not exist in simulations and the LEV flow structure is indeed stable, similar to that observed in previous

studies [e.g., Refs. 6,30,39,40]. The corresponding values of  $C_L$  and  $C_D$  in this region are denoted by  $C_{L,tr}$  and  $C_{D,tr}$ , respectively. As per the QS model [27],  $C_{L,tr} \propto \sin(2\alpha)$  and  $C_{D,tr} \propto 1 - \cos(2\alpha)$ ; see Eq. (A5).

The values of both  $C_L$  and  $C_D$  varied during the pitch perturbation and returned to values close to their original stable values after the perturbation was stopped, at around  $t/T \sim 0.75$ . The peak-to-peak variations in  $C_L$  and  $C_D$ , i.e.,  $\Delta C_L$  and  $\Delta C_D$ , respectively, changed depending on the initial angle  $\alpha_0$  even when the perturbation magnitude  $\Delta\alpha$  was kept constant. The maximum variation in  $C_L$  was observed for  $\alpha_0 = 0^\circ$ , which reduced with an increase in  $\alpha_0$ . This can be explained by considering the translational force  $F_{tr}$  and normal force  $F_{n,rot}$  acting on the wing and their contributions to the lift and drag at different wing angles. As can be seen in Eqs. (A6)–(A10), the force  $F_{n,rot}$  scales with the pitch angular velocity  $\dot{\alpha}$  and acts in the direction normal to the wing surface. Thus, the contribution of  $F_{n,rot}$  to the lift can be given by  $F_n \cos \alpha$  and that to the drag can be given by  $F_n \sin \alpha$ . Its effect on  $\Delta C_L$  and  $\Delta C_D$  can be analyzed against the mean perturbation angle, defined by

$$\bar{\alpha}_p = \frac{1}{T_p} \int_{t_1}^{t_1+T_p} \alpha dt. \quad (4)$$

The contribution of  $F_n$  to the lift, i.e.,  $F_n \cos \alpha$ , is expected to reduce with  $\bar{\alpha}_p$  and that to the drag, i.e.,  $F_n \sin \alpha$ , is expected to increase with  $\bar{\alpha}_p$ , until  $\bar{\alpha}_p = 90^\circ$ , as has been confirmed by the observations in Fig. 5(c). The figure also shows the lift and drag coefficients averaged over the period of perturbation, i.e.,  $\bar{C}_L$  and  $\bar{C}_D$ , respectively, to represent the contributions by the translational effects. The difference in the magnitudes of the translational effects and rotational effects seen in Fig. 5(c) confirms that the rotational effects have a significantly stronger influence on aerodynamic force variations during the perturbations than the translational effects do.

The peak value of  $\Delta C_D$  is observed at  $\bar{\alpha}_p \sim 75^\circ$ . To understand this trend, the values of  $C_D$  were further decomposed using the QS model into the translational component  $C_{D,tr}$  and rotational component  $C_{D,rot}$ . Note that the variations in  $C_{D,tr}$  and  $C_{D,rot}$  were not in phase. Thus, the peak-to-peak variation  $\Delta C_D$  is not the sum of  $\Delta C_{D,tr}$  and  $\Delta C_{D,rot}$ . As per the model,  $C_{D,tr}$  is proportional to  $(1 - \cos 2\alpha)$ . Its peak-to-peak variation  $\Delta C_{D,tr}$  shown in Fig. 5(d) is in line with the peak-to-peak variations in  $(1 - \cos 2\alpha)$ . It can also be seen that the contribution of  $\Delta C_{D,tr}$  is much lower compared to that of  $\Delta C_{D,rot}$ . The rotational component is derived from two parts, namely,  $F_{rot,1}$  and  $F_{rot,2}$  [see Eqs. (A6)–(A10)]. These components are dependent on the wing's geometrical parameters and  $\phi$  profile, which are constant across all cases compared in this figure. Thus, as  $\alpha$  is changed,  $F_{rot,1}$  varies proportional to  $f_\alpha \dot{\alpha}$  [see Eq. (A7)] and  $F_{rot,2}$  varies proportional to  $\dot{\alpha}|\dot{\alpha}|$  [see Eq. (A10)]. Since these components act in the wing-normal direction, their contributions to  $C_D$  are proportional to  $f_\alpha \dot{\alpha} \sin \alpha$  and  $\dot{\alpha}|\dot{\alpha}| \sin \alpha$ , respectively. Between the range  $45^\circ \leq \alpha \leq 135^\circ$ ,  $f_\alpha = \sqrt{2} \cos \alpha$  [see Eq. (A8)]. Thus, the drag contributions from  $F_{rot,1}$  and  $F_{rot,2}$  are proportional to  $(\dot{\alpha} \sin 2\alpha)$  and  $(\dot{\alpha}|\dot{\alpha}| \sin \alpha)$ , respectively.

The terms  $\dot{\alpha}$ ,  $\sin \alpha$ , and  $\sin 2\alpha$  are not in phase. Their combined effect results in the variation in  $\Delta C_{D,rot}$  with  $\bar{\alpha}_p$ , as seen in Fig. 5(d). Here, it can be seen that the variation in  $\Delta C_D$  with  $\bar{\alpha}_p$  is in line with the variations in the rotational component  $\Delta C_{D,rot}$ . The maximum value of  $\Delta C_D$  is observed around  $\bar{\alpha}_p = 75^\circ$ , similar to the maximum  $\Delta C_{D,rot}$ , followed by a gradual reduction. At very high angles,  $\bar{\alpha}_p > 100^\circ$ , the influence from the translational component contributes to the change in the trend. Nevertheless, the variations in  $C_D$  are largely influenced by the variations in the rotational effects.

Furthermore, the peak-to-peak variation in  $F_{n,rot}$  itself can be changed by changing the  $\dot{\alpha}$  profile. This can be achieved either by perturbing the pitch with a different magnitude in the same time period  $T_p$  or by changing the time period  $T_p$  for a given perturbation magnitude. Both of these are explored in the following subsections.

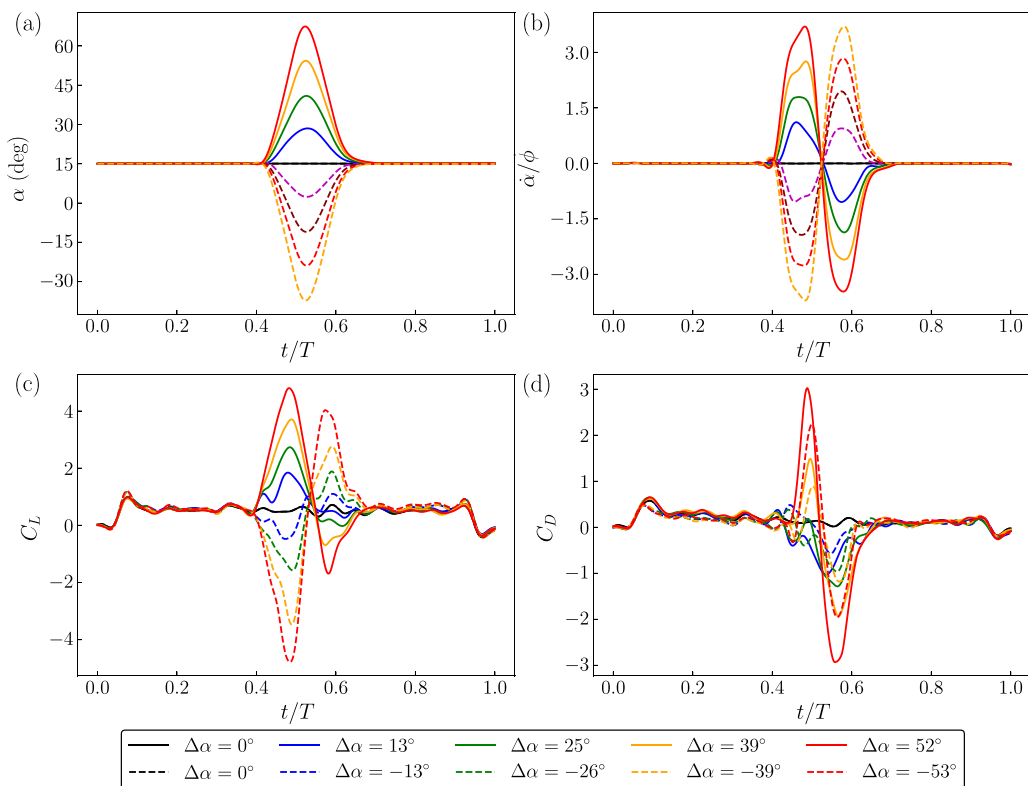


FIG. 6. The time traces of (a)  $\alpha$ , (b)  $\dot{\alpha}/\dot{\phi}$ , (c)  $C_L$ , and (d)  $C_D$  are shown for  $\alpha_0 = 15^\circ$  and various  $\Delta\alpha$ . The solid lines represent the pitch-up perturbations while the dashed lines represent the pitch-down perturbations.

### C. Effect of perturbation amplitude

The amplitude of the pitch perturbation  $\Delta\alpha$  was systematically varied to observe its effects on  $C_L$  and  $C_D$ . The initial angle and the duration of perturbation were maintained at ( $\alpha_0 = 15^\circ$ ) and ( $\tau = 0.2$ ) respectively, see Fig. 6. Both pitch-up and pitch-down perturbations were examined by varying the target  $\Delta\alpha$  in steps of  $15^\circ$ . Due to the limitations in the acceleration of the servomotors, the resulting  $\Delta\alpha$  in the actual experiments showed a variation in steps of  $\sim 13^\circ$ .

During the pitch-up perturbations,  $C_L$  was observed to rise and fall during the first half of the perturbation when  $\alpha$  increased from  $\alpha_0$  to  $\alpha_0 + \Delta\alpha$ . During the remaining half,  $C_L$  decreased to the values lower than  $C_{L,tr}$  and returned to the original value at the end of perturbation, even though  $\alpha$  was always greater than  $\alpha_0$  during this phase. This indicated that the instantaneous values of  $C_L$  depended more on the instantaneous  $\dot{\alpha}$  rather than on  $\alpha$  itself, as can be seen in Figs. 6(b) and 6(c). Similarly, during the pitch-down perturbations, the shape of the waveform of  $C_L$  was observed to be inverted, in accordance with the waveform of  $\dot{\alpha}$ . Note that the magnitudes of the peaks in the waveform are different in pitch-up and pitch-down perturbations since the translational force component contributes positively to  $C_L$  in both cases. Moreover, the peak-to-peak variations in  $C_L$  were directly proportional to  $\Delta\alpha$  in both pitch-up and pitch-down perturbations. This can be attributed to the fact that during the same  $\tau$ , achieving a higher  $\Delta\alpha$  would require a higher  $\dot{\alpha}$  and this would increase the force component  $F_{n,rot}$ . During the pitch-down perturbations, the value of  $\dot{\alpha}$  is reversed, causing  $F_{n,rot}$  also to change its direction. The net value of instantaneous  $C_L$  is an addition of the contribution from the  $F_{n,rot}$  and  $C_{L,tr}$ . The variation in  $F_{n,rot}$  is expected to be antisymmetrical during the pitch-up and return stroke, whereas  $C_{L,tr}$  remains always positive throughout this motion

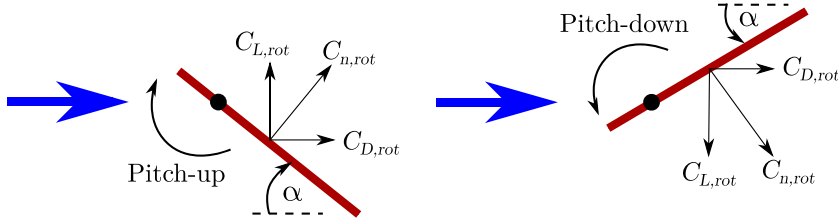


FIG. 7. Schematic shows the side view of a wing and alignment of the normal-force coefficient ( $C_n, \text{rot}$ ) during the pitch-up and pitch-down perturbations. Its components contributing to the lift ( $C_{L, \text{rot}}$ ) and drag ( $C_{D, \text{rot}}$ ) are also shown. The blue arrows represent the direction of the relative flow velocity. The black dot shows the location of the pitch axis.

due to  $\alpha$  being positive [see Eq. (A5)]. As a consequence, for pitch-up perturbations, the positive peak of  $C_L$  is greater in magnitude than its negative peak.

$C_D$  was also observed to vary similar to  $C_L$  during the pitch-up perturbations, reaching higher magnitudes with larger  $\Delta\alpha$ . However, in the pitch-down perturbations, the waveform of  $C_D$  was not inverted. This can be explained with the help of a schematic shown in Fig. 7. During a pitch-up perturbation, the angle  $\alpha$  would remain positive. Here, the normal force coefficient  $C_{n, \text{rot}}$  is pointed in the direction such that its contributions to both  $C_L$  and  $C_D$  will be positive. However, since the initial angle  $\alpha_0$ , in this case, is small, the value of  $\alpha$  during the pitch-down perturbation would be negative. Hence, the normal force would act in the downward direction, contributing to the negative  $C_L$ . However, its component contributing to the drag would still be along the same direction as the flow, as shown in the schematic. This would cause  $C_D$  to be positive even in the pitch-down perturbation. In the later half of the perturbation, the wing returns to its original position. During this time, the sign of  $\dot{\alpha}$  would be reversed, causing  $C_{n, \text{rot}}$  also to reverse its direction. Thus, its contribution to  $C_L$  and  $C_D$  would also have reverse signs.

Pitch perturbations on a linearly translating wing are known to experience the phenomenon of dynamic stall when the angle of attack exceeds the static stall angle [18,43–45]. During rapid excursions in pitch angle, dynamic stall contributes to hysteresis in the variation in  $C_L$  as a function of  $\alpha$ . The same effect was also investigated in the case of a rotationally translating wing here, as shown in Fig. 8(a). Here, the data for the instantaneous  $C_L$  for pitch-up perturbations from Fig. 6 have been plotted in relation to the instantaneous  $\alpha$ . The black line in Figs. 8(a) and 8(b) represent the stabilized  $C_L$  values as functions of  $\alpha$  for an unperturbed wing at different angles. Nevertheless, even in the case of rotating wings, the pitch perturbations were observed to introduce hysteresis in  $C_L$  around the measurements for the unperturbed cases. The size of the hysteresis loop increased with  $\Delta\alpha$ . The QS model predictions show a reasonable match with most  $C_L$  values.

The large deviations in the experimental data from the QS model predictions observed in the case of  $\Delta\alpha = 53^\circ$  in this figure are not observed when plotted as functions of time; see the same data plotted in Fig. 3(b). When plotted as functions of time, the difference between the data and the QS model predictions is within the range of uncertainty, as is mentioned in Sec. II C. When plotted as functions of  $\alpha$ , the deviations appear to be larger at a given  $\alpha$  due to the slight time delay observed in the experimental data with respect to the QS predictions. For the case  $\Delta\alpha = 53^\circ$ , the wing experiences the highest pitch-rotation rate in the explored range ( $\dot{\alpha}_{\text{max}}/\dot{\phi} \sim 4$ ). Thus, a small time delay, in this case, would result in a larger change in  $\alpha$  compared to that in other cases. For lower  $\Delta\alpha$ , the deviations are lower due to a lower pitch rate.

The QS model is further used to decompose  $C_L$  into the contributions from translational effects ( $C_{L, \text{tr}}$ ) and rotational effects ( $C_{L, \text{rot}}$ ), as shown in Fig. 8(b). Note that in Fig. 8(b), dashed lines represent  $C_{L, \text{tr}}$  and dash-dot lines represent  $C_{L, \text{rot}}$ . Since the translational lift coefficient is only a function of  $\alpha$  [see Eq. (A5)], it was expected to follow the  $C_L$ - $\alpha$  relation for the unperturbed case, as confirmed by the close overlap of all  $C_{L, \text{tr}}$  values during the perturbations with the line representing

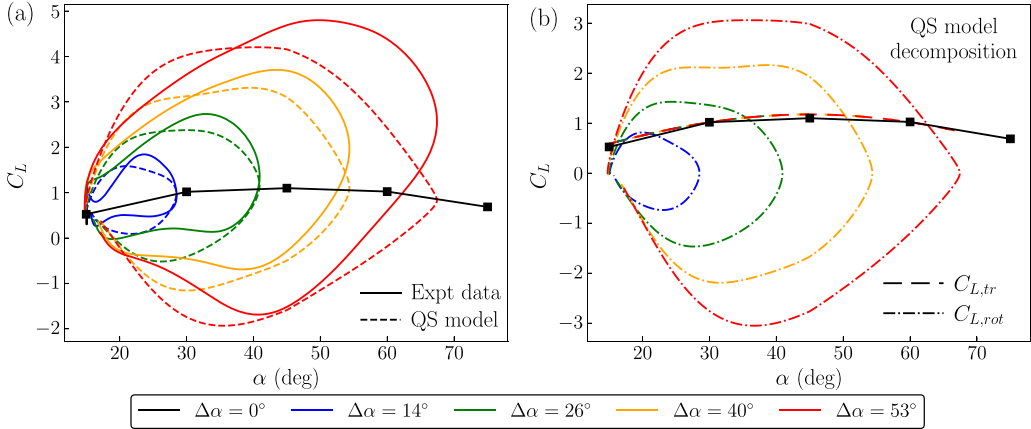


FIG. 8. Variations in  $C_L$  with  $\alpha$  are shown in panel (a) for various  $\Delta\alpha$ , where the solid lines represent experimental data and the dashed lines represent the QS model predictions. The black line shows the data without any pitch perturbations. The QS model predictions are further decomposed in panel (b) showing the translational component  $C_{L,tr}$  (dashed lines) and rotational component  $C_{L,rot}$  (dash-dot lines). In these cases,  $\Delta\alpha$  is varied while maintaining  $\alpha_0 = 15^\circ$  and  $\tau = 0.2$ .

the unperturbed wing at various angles. The deviation from this relation is introduced purely by the rotational effects since all  $C_{L,rot}$  curves show a large hysteresis increasing in size with  $\Delta\alpha$ . As the rotational forces scale with  $\dot{\alpha}$  [as per Eqs. (A6)–(A10)], a higher  $\dot{\alpha}$  required for higher  $\Delta\alpha$  results in higher magnitudes of  $C_{L,rot}$ , and hence, in larger hysteresis loops. Overall, this analysis reveals that the quasisteady component related to the pitch-rotational velocity is the reason behind the hysteresis observed in  $C_L$ .

While the aerodynamics of an unperturbed revolving wing are characterized by a stable 3D LEV structure, all pitch perturbations in this study exhibit significantly higher rotational effects dominating the perturbed-wing flow profile and performance. It can be hypothesized that at lower pitch rates, the stability of the LEV might not be disturbed by perturbations and hence, the forces acting on the wing as a result of the stable LEV would dominate over the rotational effects. This was investigated using computational simulations for cases with low amplitudes of pitch-up perturbations, i.e.,  $\Delta\alpha = 2.7^\circ, 5.3^\circ, 8.1^\circ$ , and  $11.6^\circ$  when the initial angles of the wing were set to  $\alpha_0 = 15^\circ, 45^\circ$ , and  $75^\circ$ . The normalized duration of perturbation  $\tau = 0.2$  was maintained to be constant across all these cases.

To quantify the magnitude of force perturbations with respect to the stable-LEV-generated forces, the variations in both lift and drag coefficients (i.e.,  $\Delta C_L$  and  $\Delta C_D$ ) were normalized with the mean lift and drag coefficients (i.e.,  $\bar{C}_{L,tr}$  and  $\bar{C}_{D,tr}$ ), respectively, of the unperturbed wing at the respective  $\alpha_0$ . Accordingly, the quantities  $\Delta C_L/\bar{C}_{L,tr}$  and  $\Delta C_D/\bar{C}_{D,tr}$  were observed to vary with  $\Delta\alpha$ , as shown in Figs. 9(a) and 9(b). As expected, the force perturbations increased with  $\Delta\alpha$  due to the increased pitch-rotation rates. These values are also found to be dependent on  $\alpha_0$ . The values of  $\Delta C_L$  are expected to decrease with  $\alpha_0$  as the normal force generated by the rotational effects will be oriented more along the drag at higher wing angles. The value of  $\bar{C}_{L,tr}$  is maximum at  $\alpha_0 = 45^\circ$ , as discussed in Sec. III A. Thus, the variation in  $\Delta C_L/\bar{C}_{L,tr}$  shows lower values at  $\alpha_0 = 45^\circ$  than those from the other two angles compared here. Similarly,  $\Delta C_D$  is expected to increase with  $\alpha_0$  due to the increased contribution from the rotational effects.  $\bar{C}_{D,tr}$  is also expected to increase with  $\alpha_0$  as discussed in Sec. III A. Due to a higher rise in  $\bar{C}_{D,tr}$  than in  $\Delta C_D$ , the ratio  $\Delta C_D/\bar{C}_{D,tr}$  is observed to decrease from  $\alpha_0 = 15^\circ$  to  $45^\circ$  with a minimal change at  $75^\circ$ . The higher increase in  $\bar{C}_{D,tr}$  at high wing angles indicates that the 3D LEV contribution might be significant at those angles.

At very low values of  $\Delta\alpha$ , the values of  $\Delta C_L/\bar{C}_{L,tr}$  and  $\Delta C_D/\bar{C}_{D,tr}$  are less than 1. This implies that, during very-low amplitude pitch perturbations, the peak oscillations  $\Delta C_L$  and  $\Delta C_D$  caused by

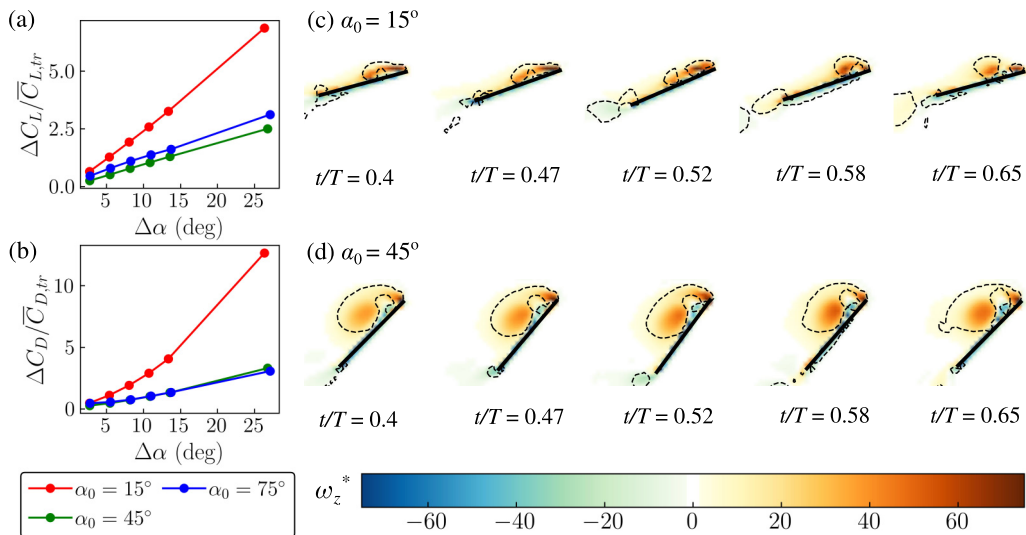


FIG. 9. The variations in (a)  $C_L$  during a perturbation scaled with the quasisteady  $C_L$  of an unperturbed wing and (b)  $C_D$  during a perturbation scaled with the quasisteady  $C_D$  of an unperturbed wing are shown as functions of  $\Delta\alpha$  for three initial angles,  $\alpha_0 = 15^\circ$ ,  $45^\circ$ , and  $75^\circ$ . The normalized vorticity contours on the midplane passing through the midspan of the wing at five time steps during a pitch-up perturbation are shown in panel (c) for  $\alpha_0 = 15^\circ$  and panel (d) for  $\alpha_0 = 45^\circ$ . The dashed lines represent the contours of the constant  $Q$  criterion.  $\Delta\alpha = 8.1^\circ$  and  $\tau = 0.2$  were maintained to be constant in both panels (c) and (d).

the rotational effects are less than the stable-LEV-generated values  $\overline{C}_{L,tr}$  and  $\overline{C}_{D,tr}$ , respectively. For  $\alpha_0 = 15^\circ$ , this is observed at  $\Delta\alpha < 4^\circ$ , whereas for  $\alpha_0 = 45^\circ$ , this is observed at  $\Delta\alpha < 10^\circ$ . One explanation for this could be that, at lower initial angles, the LEV is relatively weak and can be easily disturbed by small perturbations as compared to higher initial angles where the LEV is stronger. To investigate those effects on the LEV, flow structures on a cross-sectional plane through the midspan of the wing with  $\alpha_0 = 15^\circ$  and  $\alpha_0 = 45^\circ$  were compared, as shown in Figs. 9(c) and 9(d). The pitch-rotation rate was chosen to be the same by maintaining  $\Delta\alpha = 8.1^\circ$  and  $\tau = 0.2$  constant. Five different time steps during a perturbation are shown here. Indeed, it can be seen that the LEV formed with  $\alpha_0 = 15^\circ$  is much smaller and weaker than that with  $\alpha_0 = 45^\circ$ . As a result, for the same pitch-rotation rate, the weaker LEV with  $\alpha_0 = 15^\circ$  is observed to be disturbed at  $t/T = 0.52$  and  $t/T = 0.65$ . The stronger LEV with  $\alpha_0 = 45^\circ$  is only minimally affected, without experiencing any split. These observations indicate that the rotational effects dominate the aerodynamics of the perturbed wing at higher pitch rates. At lower pitch rates, strong 3D effects that stabilize the LEV over a revolving wing are more dominant. The values of those rotation rates at which the transition from the LEV-dominant to the rotation-dominant flow occurs depend on the initial angle of the revolving wing.

#### D. Effect of the duration of perturbation

The pitch-rotation effects can also be changed by varying the duration of perturbation  $T_p$ . To investigate those effects, the instantaneous values of  $C_L$  and  $C_D$  for two values of the normalized duration of perturbation (i.e.,  $\tau = 0.2$  and  $0.4$ ) are compared in Fig. 10. For a chosen amplitude of perturbation  $\Delta\alpha$ , the hysteresis loop obtained for  $\tau = 0.4$  is observed to be narrower than that for  $\tau = 0.2$ . This is because, for the same amplitude, the longer duration would require a lower  $\dot{\alpha}$ . This would result in lower rotational effects in terms of the values of  $F_{n,rot}$ , as discussed earlier. In this figure, for a similar target  $\Delta\alpha$ , the actual  $\Delta\alpha$  achieved is slightly different for  $\tau = 0.2$  and  $0.4$  due to the difference in the servo motor's acceleration in the two cases. With a lower pitch acceleration

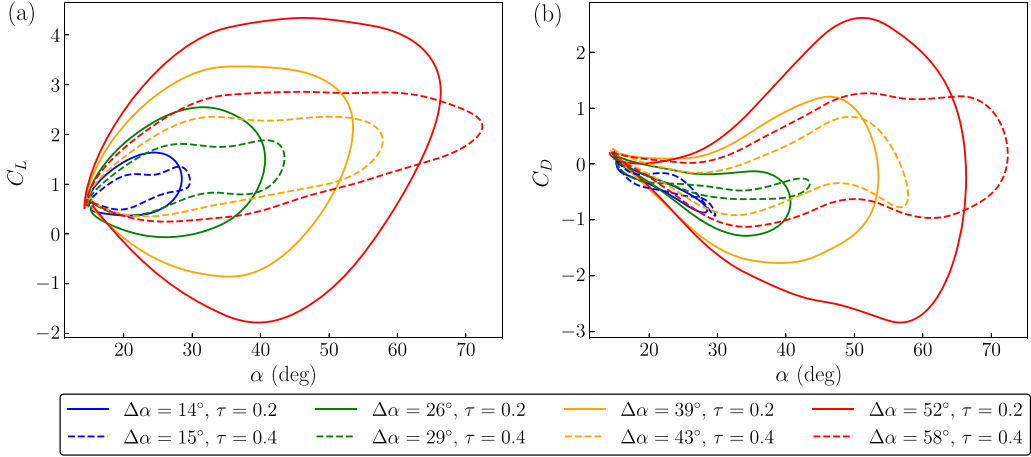


FIG. 10. Instantaneous values of (a)  $C_L$  and (b)  $C_D$  are plotted against the instantaneous  $\alpha$  for various  $\Delta\alpha$ . Here, solid lines represent  $\tau = 0.2$  and dashed lines represent  $\tau = 0.4$ . In all cases,  $\alpha_0 = 15^\circ$ .

with  $\tau = 0.4$ , the wing was able to reach  $\Delta\alpha$  closer to the target value. Nevertheless, the lower values of  $\dot{\alpha}$  resulted in lower hysteresis effects, as is evident from the figure.

In conclusion, hysteresis does appear in the pitch-perturbed revolving wing, similar to that observed in the pitch-perturbed linearly translating wings. In the case of revolving wings at a constant Reynolds number, the hysteresis is due to the effects of the pitch-rotation velocity when the other parameters affecting  $F_{n,\text{rot}}$ , such as the Rossby number and pitch-axis location, are maintained to be constant. Thus, a smaller amplitude of perturbation during the same duration or a larger duration for the same amplitude would both reduce the hysteresis effects. Hysteresis was observed in all perturbation rates examined in this study, i.e.,  $\Delta\dot{\alpha}/\dot{\phi} \geq 1$ .

### E. Effect of pitch-axis location

The above results indicate that large variations in the instantaneous  $C_L$  and  $C_D$  can be controlled by controlling the rotational effects. The force  $F_{n,\text{rot}}$  due to the rotational effects has two parts, namely,  $F_{\text{rot},1}$  and  $F_{\text{rot},2}$ , defined as

$$F_{\text{rot},1} = f_\alpha f_r (0.927 - 0.558 \text{Re}^{-0.1577}) \dot{\phi} \dot{\alpha} \int_0^R c(r)^2 r dr \quad \text{and} \quad F_{\text{rot},2} = 2.67 \rho \dot{\alpha} |\dot{\alpha}| \int_{\text{LE}}^{\text{TE}} r x |x| dx, \quad (5)$$

where  $f_\alpha$  is the factor dependent on the instantaneous  $\alpha$ ,  $f_r$  is the factor due to the pitch-axis location, and  $x$  is the chordwise distance measured from the pitch axis and is positive in the direction towards the trailing edge (TE). Various terms in these equations are described in Eqs. (A7)–(A10). The factor  $f_r$  in  $F_{\text{rot},1}$  changes with the pitch axis location. The part  $F_{\text{rot},2}$  changes with  $x$ , which is directly dependent on the distribution of the wing area with respect to the pitch axis. The value of  $F_{\text{rot},2}$  will be 0 if the pitch axis is located at the center of the wing chord. Hence, both  $F_{\text{rot},1}$  and  $F_{\text{rot},2}$  change with a change in the pitch-axis location. Consequently, the pitch axis location might affect the overall wing performance.

Computational simulations were used to study two cases, one with the pitch axis located at the normalized location of  $\hat{x}_{\text{pa}} = x_{\text{pa}}/c = 0.2$  and the other with the pitch axis located at  $\hat{x}_{\text{pa}} = 0.5$ . Here,  $x_{\text{pa}}$  is the chordwise distance of the pitch axis measured from the leading edge. Note that the CFD predictions for both  $C_L$  and  $C_D$  showed a better match with the QS model predictions than the experimental data did (see Fig. 3). Hence, the CFD simulations for studying the pitch-axis location effects provided a better decomposition of forces for further analysis. The values  $\alpha_0 = 15^\circ$ ,

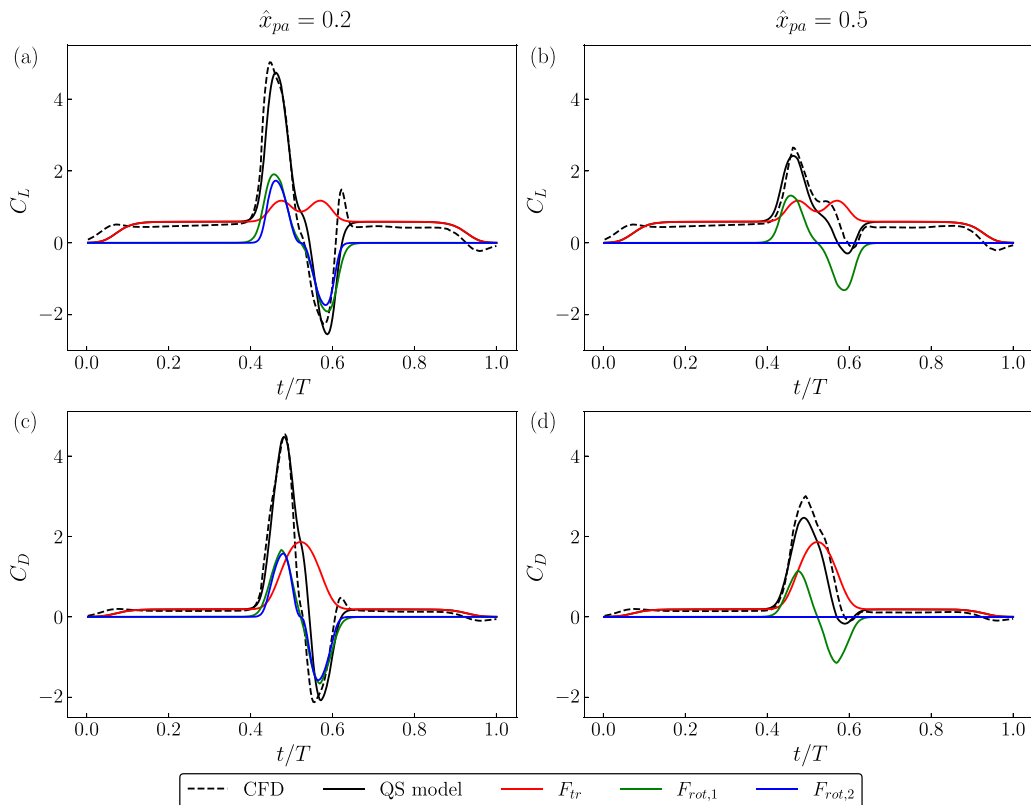


FIG. 11. Panels (a) and (c) show the time traces of  $C_L$  and  $C_D$ , respectively, with the normalized chordwise location of the pitch axis  $\hat{x}_{pa} = 0.2$ , whereas panels (b) and (d) show the same time traces with  $\hat{x}_{pa} = 0.5$ . In both cases,  $\alpha_0 = 15^\circ$ ,  $\Delta\alpha = 52^\circ$ , and  $\tau = 0.2$ . The dashed lines represent the CFD results while the solid lines represent the QS model estimations. Here, the force coefficients ( $C_L$  and  $C_D$ ) have been decomposed into the translational effects due to  $F_{tr}$  (red) and the rotational effects due to  $F_{rot,1}$  (green) and  $F_{rot,2}$  (blue). The red and black solid lines overlap each other before and after the perturbation.

$\Delta\alpha = 52^\circ$ , and  $\tau = 0.2$  were maintained to be the same in both simulated cases. The time traces of  $C_L$  and  $C_D$  for the two cases are shown in Fig. 11.

In this figure, the predictions of CFD match reasonably well with the QS model estimates. The net  $C_L$  and  $C_D$  are decomposed into the contributions from the translational effects ( $F_{tr}$ ) from Eq. (A5), rotational effects estimated from the Kutta-Joukowski theory ( $F_{rot,1}$ ) from Eq. (A7), and rotational effects due to the local drag force normal to the wing surface ( $F_{rot,2}$ ) from Eq. (A10). Since the translation effects are independent of the pitch axis location, the resulting time traces of the translational force coefficients are the same in both cases. However, the component  $F_{rot,2}$  is 0 in the case with  $\hat{x}_{pa} = 0.5$ , as predicted. Therefore, the variations in the net values of  $C_L$  and  $C_D$  are reduced. Note that both rotational components  $F_{rot,1}$  and  $F_{rot,2}$  depend on  $\dot{\alpha}$ . Hence, their mean value is 0. As a result, the average values of  $C_L$  and  $C_D$  only depend on the average of the translational components. Thus, the change in the pitch-axis location does not affect the average wing performance; however, it does affect the instantaneous variations in  $C_L$  and  $C_D$ .

#### IV. DISCUSSION

The results discussed above showed that both  $C_L$  and  $C_D$  vary during the pitch perturbation and returned to their stable values after the perturbation. In the case of rotating and flapping wings, the



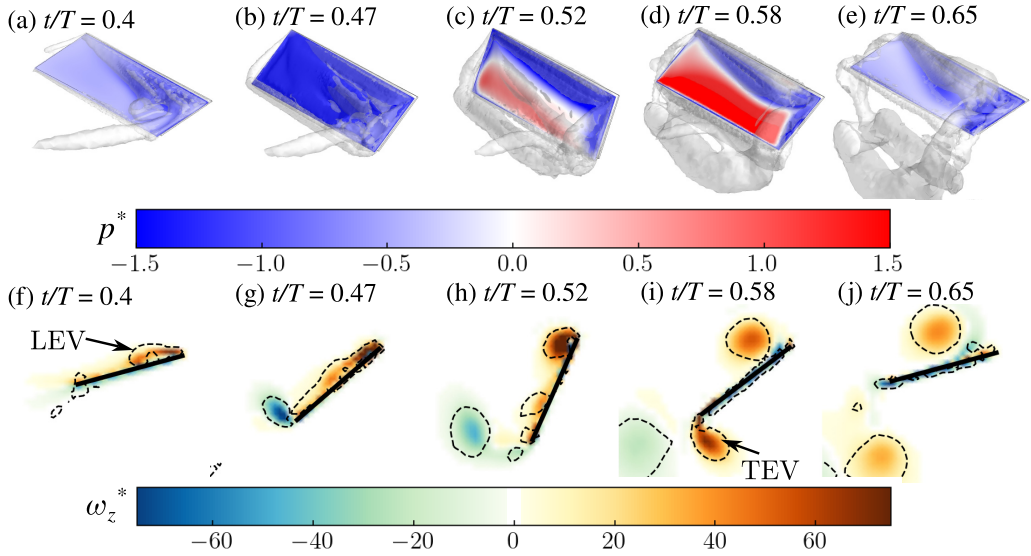


FIG. 12. For the wing during its pitch perturbation with  $\alpha_0 = 15^\circ$ ,  $\Delta\alpha = 52^\circ$ ,  $\tau = 0.2$ , and  $\hat{x}_{pa} = 0.2$ , the top row (a)–(e) shows the normalized pressure ( $p^*$ ) contours on the wing’s suction surface at various time steps. The vortical structures are shown by the semitransparent isosurfaces of the constant  $Q$  criterion. The bottom row (f–j) shows the normalized spanwise vorticity ( $\omega_z^*$ ) contours over a cross-sectional plane passing through the center of the wingspan at the same time steps as in the top row. Here, the dashed lines represent the constant  $Q$  criterion. Refer to Figs. 11(a) and 11(c) for time traces of  $C_L$  and  $C_D$ , respectively.

vortical structures are commonly observed to have a large influence on  $C_L$  and  $C_D$  variations. Hence, to analyze the effects of the flow structures around the wing on the wing performance during the pitch perturbation, the normalized wing-surface pressure [ $p^* = p/(0.5\rho U_{ref}^2)$ ] contours were plotted at various time steps along with the flow structures identified by the constant  $Q$  criterion [46], as shown in Fig. 12.

Before the start of the pitch-perturbation, the wing had revolved around the sweep axis with a constant angular velocity  $\dot{\phi} = 20^\circ/s$  and angle  $\alpha_0 = 15^\circ$ . A conical LEV was formed, which remained attached to the wing surface. As can be seen in Fig. 12(a), high magnitudes of suction pressure (i.e., negative  $p^*$ ) are found to be beneath the LEV. Since the pitching axis in this case is closer to the leading edge, when the wing starts pitching up, a major part of the wing below the pitching axis starts moving downward. Due to the net downward resultant velocity, the magnitudes of suction on the wing surface increase significantly, for example in Fig. 12(b). This rise in the suction magnitude is responsible for the higher  $C_L$  observed during the pitch-up motion [see Fig. 11(a)]. When the pitch motion decelerates and the wing starts pitching down, the net relative velocity of the lower region of the wing is upwards, which results in the positive  $p^*$  in this region [see Figs. 12(c) and 12(d)]. Hence, the net normal force on the wing acts downwards, due to which a negative  $C_L$  is observed [see Fig. 11(a)]. When the perturbation ends [in Fig. 12(e)], the suction pressure on the wing surface is recovered.

The flow structures on the wing undergo significant changes due to pitch perturbation. For better clarity, the normalized spanwise vorticity [ $\omega_z^* = \omega_z(0.75R)/U_{ref}$ ] contours are plotted on a cross-sectional plane passing through the wing’s midspan, as shown in Figs. 12(f)–12(j). During the pitch-up motion, a strong trailing-edge vortex starts to develop, which is separated from the wing at the end of the pitch-up motion at  $t/T = 0.52$ . Simultaneously, during the pitch-up motion, the LEV is disturbed and is spread over most of the wing suction surface, remaining close to the surface. During the pitch-up motion, the relative velocity of the fluid separating at the leading edge is lower than that

at the end of the pitch-up motion at  $t/T = 0.52$ . Hence, the shear layer on the leading edge forms a stronger LEV at  $t/T = 0.52$  than that during the pitch-up motion. The relative velocity of the separating fluid further increases during the wing's pitch-down motion and feeding of vorticity in the LEV increases. Consequently, the LEV grows in size and is also lifted away from the wing surface, as can be seen in Figs. 12(i) and 12(j). Moreover, an upward motion of the trailing edge also creates a shear, thereby forming a trailing-edge vortex (TEV) of the same-sign vorticity as that of the LEV, but on the pressure side of the wing. At the end of the pitch perturbation [in Fig. 12(j)], both LEV and TEV move away from the respective wing surfaces. At this time step, the flow structures around the wing are very different from those before the start of the perturbation. However, the values of  $C_L$  and  $C_D$  are observed to be similar before and immediately after the perturbation. Hence, the observed changes in the flow structures only minimally affect the forces on the wing in the explored range of pitch-rotation rates (the normalized maximum pitch rate range:  $\dot{\alpha}_{\max}/\dot{\phi} < 4$ ) in this study. Chen *et al.* [26] attributed the changes in  $C_L$  to the vortex stretching and tilting that occurred during the perturbation. However, the vortex stretching and tilting may not completely explain the changes in  $C_L$  since the effects of the local drag affecting the wing-surface pressures were not considered.

The wing-surface pressures are more related to the wing motion, which can be explained by the rotational effects in the QS model. As per the QS model, the translational effects are proportional to the instantaneous angle  $\alpha$  and the rotational effects are proportional to the instantaneous pitch-angular velocity  $\dot{\alpha}$ . Since the pitch perturbation follows a symmetric profile in  $\alpha$ , the mean value of  $\dot{\alpha}$  is expected to be 0. Hence, the mean value of  $C_L$  (i.e.,  $\bar{C}_L$ ) will be independent of  $\dot{\alpha}$  and will depend only on the mean  $\alpha$  during the perturbation (i.e.,  $\bar{\alpha}_p$ ). The peak-to-peak variations in  $C_L$  (i.e.,  $\Delta C_L$ ) will depend on the peak-to-peak variations in  $\dot{\alpha}$  (i.e.,  $\Delta\dot{\alpha}$ ). This is shown by plotting  $\bar{C}_L$  against  $\bar{\alpha}_p$  and  $\Delta C_L$  against  $\Delta\dot{\alpha}/\dot{\phi}$  for the data obtained from various  $\alpha_0$ ,  $\Delta\alpha$ ,  $\tau$ , and both pitch-up and pitch-down perturbations, as shown in Fig. 13.

The values of  $\bar{C}_L$  in all cases fit well along the function  $\sin(2\bar{\alpha}_p)$  for the translational component in the QS model, as can be seen in Fig. 13(a). Similarly, all values of  $\Delta C_L$  for a given  $\alpha_0$  show a monotonous increase with  $\Delta\dot{\alpha}$ , as shown in Fig. 13(b). However, for different  $\alpha_0$ , the curves shift, indicating that  $\Delta C_L$  must also depend on the instantaneous angle. Revising the QS model for rotational effects reveals that  $\Delta C_L \propto \Delta F_{\text{rot}} \cos(\alpha)$ . Moreover,  $F_{\text{rot}}$  must be a quadratic function of  $\dot{\alpha}$  (see Eqs. (A6)–(A10)). Hence,  $\Delta C_L \propto (\Delta\dot{\alpha}/\dot{\phi}) \cos \bar{\alpha}_p$ . This is verified by plotting  $\Delta C_L$  as a function of  $(\Delta\dot{\alpha}/\dot{\phi}) \cos \bar{\alpha}_p$  in Fig. 13(c). Most values collapse along a curve roughly approximated by a quadratic least-square fit. This clearly shows that the instantaneous variations in  $C_L$  depend on both the pitch-rotational velocity and the mean perturbation angle.

Note that, in all perturbed cases,  $\Delta\dot{\alpha} > \dot{\phi}$ . Hence, the pitch-rotational effects on  $C_L$  are significantly higher than the translational effects. The collapse of data from various cases in Fig. 13(c) demonstrates that, despite undergoing pitch perturbations with different initial angles, amplitudes, and duration, the same  $(\Delta\dot{\alpha}/\dot{\phi}) \cos \bar{\alpha}_p$  should result in the same variations in  $C_L$ . In conclusion, the instantaneous forces on the wing are highly sensitive to the pitch-rotation velocity and the mean perturbation angle, whereas the average performance is dependent on the translational effects only.

Finally, the coefficient of power transferred from the fluid to the wing was calculated as

$$C_P = \frac{\tau_y \dot{\phi} + \tau_z \dot{\alpha}}{0.5 \rho U_{\text{ref}}^3 A}, \quad (6)$$

where  $\tau_y$  and  $\tau_z$  are the torques around the flapping and pitching axes, respectively. Accordingly, the flapping and pitching powers can be separated as  $C_P = C_{P,\text{flap}} + C_{P,\text{pitch}}$ . For various values of  $\alpha_0$  and  $\Delta\alpha$  explored in this work, the mean power transfer coefficients  $\bar{C}_{P,\text{flap}}$  and  $\bar{C}_{P,\text{pitch}}$  during the perturbation were computed for all cases with  $\tau = 0.2$  and  $\hat{x}_{\text{pa}} = 0.2$ . The values of those power coefficients were plotted as contours on the maps of  $\alpha_0$  and  $\Delta\alpha$ , as shown in Fig. 14. The flapping power is observed to be dependent on both  $\alpha_0$  and  $\Delta\alpha$ , whereas the pitching power is primarily a function of  $\Delta\alpha$ , virtually independent of  $\alpha_0$ . This is because the flapping torque  $\tau_y$  depends on the

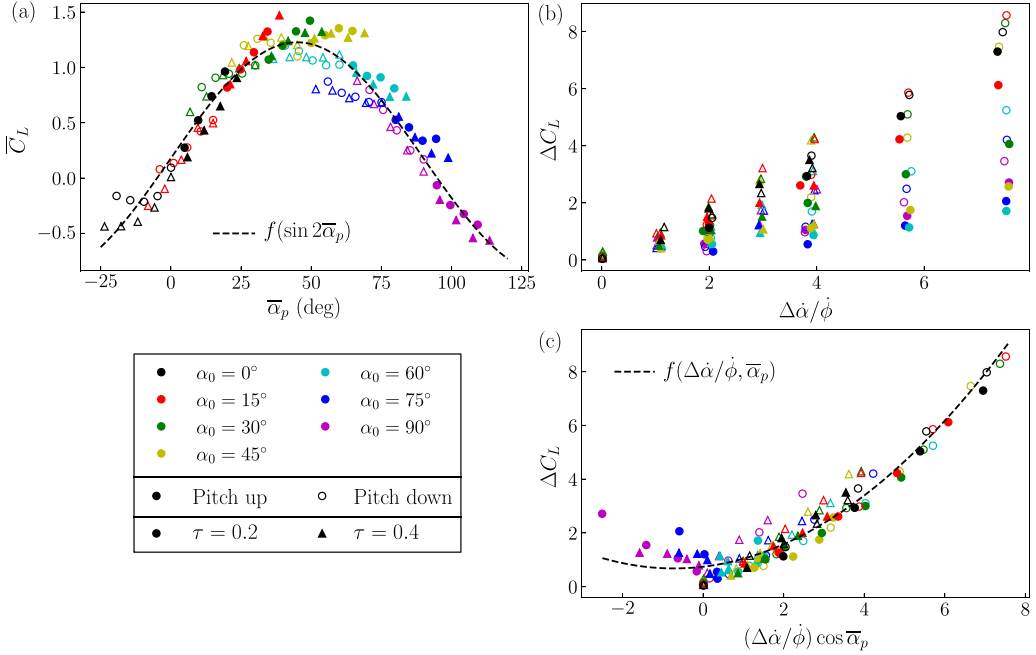


FIG. 13. For various  $\alpha_0$ ,  $\Delta\alpha$ , and  $\tau$ , the mean lift coefficient ( $\bar{C}_L$ ) values are plotted as a function of the mean perturbation angle  $\bar{\alpha}_p$  in panel (a). The peak-to-peak variation ( $\Delta C_L$ ) during the perturbation is plotted as a function of the normalized peak-to-peak perturbation angular velocity  $\dot{\alpha}/\dot{\phi}$  in panel (b) and as a function of  $(\Delta\dot{\alpha}/\dot{\phi}) \cos \bar{\alpha}_p$  in panel (c). The dashed line in panel (a) shows a least-square fit to the function  $\sin(2\bar{\alpha}_p)$ . The dashed line in panel (c) shows a least-square fit to a quadratic function of  $(\Delta\dot{\alpha}/\dot{\phi}) \cos \bar{\alpha}_p$ .

drag acting on the wing that changes with both  $\alpha_0$  and  $\Delta\alpha$ . However, the pitching torque  $\tau_z$  depends mainly on the rotational force  $F_{n,\text{rot}}$ , which is a function of  $\dot{\alpha}$  as discussed above.

The region bounded by  $10^\circ \leq \alpha_0 \leq 30^\circ$  and  $-20^\circ \leq \Delta\alpha \leq -50^\circ$  in Fig. 14(a) might be of interest since it shows positive power transfer from the fluid to the wing. This indicates the possibility of the wing being self-propelled about the flapping axis. It should be noted that these values are within the uncertainty of the experiments and the QS model does not predict the positive

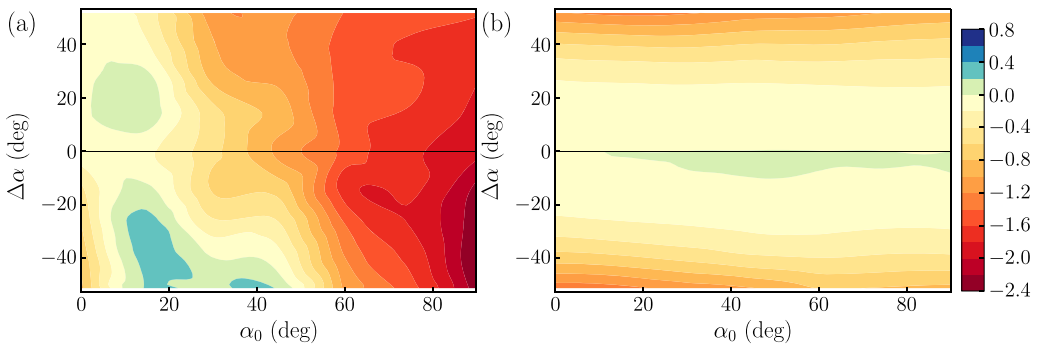


FIG. 14. The contours of the time-averaged coefficients of (a) flapping power ( $\bar{C}_{P,\text{flap}}$ ) and (b) pitching power ( $\bar{C}_{P,\text{pitch}}$ ) are shown on the maps of  $\alpha_0$  and  $\Delta\alpha$  for the cases with  $\tau = 0.2$  and  $\hat{x}_{\text{pa}} = 0.2$ .

power transfer in this region. Nevertheless, the possibility of reduced drag or improved flapping efficiency around this region may be explored in future.

## V. CONCLUSIONS

The effects of pitch perturbations on a revolving wing were studied, both experimentally and numerically, by providing a single pitch perturbation during its rotation about the span-normal axis with a constant angular velocity. The initial angle, amplitude and duration of perturbation were systematically varied. In the absence of any pitch perturbation, wings rotating at a constant Reynolds number and set at a constant angle are known to experience constant lift and drag due to the stable attachment of the leading-edge vortex. However, in this work, the stability of the lift and drag forces was observed to be severely affected during pitch perturbation. The magnitudes of changes in the lift and drag coefficients were found to be sensitive to the initial angle.

The applicability of the quasisteady (QS) model developed for flapping wings by Ref. [27] was examined to predict forces on the pitch-perturbed revolving wings. Irrespective of the highly unsteady nature of the flow around the pitch-perturbed wing, its lift and drag coefficients could be predicted remarkably well using the QS model. Accordingly, the effects of pitch perturbations were decomposed into translational and rotational effects. The large-amplitude variations in the lift and drag during perturbations on a revolving wing were shown to be associated predominantly with the rotational effects explained by the QS model. These rotational effects were dependent on a combined function of the mean pitch angle and the pitch-rotational velocity, which was modified by changing the amplitude and duration of perturbations in different sets of experiments. An increase in the pitch-rotational velocity was found to result in an increase in the hysteresis in the variation in the lift as a function of the wing angle. The hysteresis was found to be due to the changes in the circulation around the wing and the local drag force, both being related to the pitch-rotational velocity. Moreover, the rotational effects were found to be highly sensitive to the pitch-axis location. Thus, the oscillations in the lift and drag coefficients during the perturbations could be decreased by moving the pitch axis closer to the wing's center of mass. However, the mean lift and drag would remain unaffected, since they were dependent only on the translational effects. The mean lift coefficient was only a function of the mean perturbation angle, whereas the peak-to-peak variations in the lift coefficient depended on both the pitch-perturbation velocity and the mean perturbation angle.

Furthermore, the lift and drag were observed to return to their stable values at  $t/T \sim 0.75$ , irrespective of the significant changes in the flow structure around the wing. Thus, the quasisteady effects due to pitch rotation dominated the instantaneous forces in most cases. With sufficiently low pitch rates, the stability of the LEV over a wing was minimally disturbed and the LEV-generated forces dominated over the rotational effects. The values of such pitch rates were found to be highly dependent on the initial wing angle. Finally, the analysis of the power transfer between the fluid and the wing showed that the pitching power relied only on the perturbation velocity, whereas the flapping power relied on both the initial angle and the perturbation velocity. Interestingly, some pitch-down perturbations showed a possibility of improved power economy, which may be explored in detail in future.

## ACKNOWLEDGMENTS

The authors acknowledge the Technical Support Group (TSG) at UNSW Canberra for their assistance with equipment and advice for the fabrication of the flapping wing apparatus. This work was supported by the Air Force Office of Scientific Research (Grant No. FA2386-20-1-4084).

## APPENDIX: QUASISTEADY MODEL OF LEE *ET AL.* [27]

According to this model, the lift ( $L$ ) and drag ( $D$ ) forces on a wing can be decomposed as

$$L = L_{tr} + (F_{n,rot} + F_a) \cos \alpha \quad \text{and} \quad D = D_{tr} + (F_{n,rot} + F_a) \sin \alpha, \quad (A1)$$

respectively. Here,  $L_{tr}$  and  $D_{tr}$  are the lift and drag components due to the wing's rotational translation, i.e., the sweep motion,  $F_{n,rot}$  is the force due to the wing's rotation about the pitch axis,  $F_a$  is the force due to the added mass and  $\alpha$  is the wing's angle of attack. Since the added-mass forces were subtracted from the total forces in experiments and CFD, the same were neglected in the calculations using the QS model. The translational components are given by

$$\begin{aligned} L_{tr} &= f_{AR,tr} f_{Ro,tr} C_{L,tr} \left( 0.5 \rho \dot{\phi}^2 \int_0^R c(r) r^2 dr \right) \quad \text{and} \\ D_{tr} &= f_{AR,tr} f_{Ro,tr} C_{D,tr} \left( 0.5 \rho \dot{\phi}^2 \int_0^R c(r) r^2 dr \right), \end{aligned} \quad (A2)$$

where  $f_{AR,tr}$  is the aspect ratio correction factor:

$$f_{AR,tr} = 32.9 - 32AR^{-0.00361}, \quad (A3)$$

and  $f_{Ro,tr}$  is the Rossby number correction factor:

$$f_{Ro,tr} = -0.205 \tan^{-1}[0.587(Ro - 3.105)] + 0.87. \quad (A4)$$

Note that these and other following values in this model are tuned by Lee *et al.* [27] based on a number of CFD results obtained by varying AR, Re, Ro, and  $x_{rot}$ . Here, the Rossby number has been defined as  $Ro = R_g/c$ , where  $R_g$  is the wing's radius of gyration. Similarly, Re in this model has also been defined based on the velocity at  $R_g$ . The translational lift and drag coefficients are dependent on the Reynolds number (Re) and  $\alpha$  and are given by

$$\begin{aligned} C_{L,tr} &= (1.966 - 3.94Re^{-0.429}) \sin(2\alpha) \quad \text{and} \\ C_{D,tr} &= (0.031 + 10.48Re^{-0.764}) + (1.873 - 3.14Re^{-0.369})[1 - \cos(2\alpha)], \end{aligned} \quad (A5)$$

respectively. The normal force due to rotational effects,  $F_{n,rot}$ , can be considered as the sum of two components,

$$F_{n,rot} = F_{rot,1} + F_{rot,2}, \quad (A6)$$

where  $F_{rot,1}$  is due to the circulation around the wing as a result of pitch rotation, as per the conventional Kutta-Joukowski theory, and  $F_{rot,2}$  is due to the local drag force acting on the wing as a result of the wing's instantaneous pitch rotation. The force  $F_{rot,1}$  can be predicted by

$$F_{rot,1} = f_\alpha f_r (0.927 - 0.558Re^{-0.1577}) \dot{\phi} \dot{\alpha} \int_0^R c(r) r^2 r dr. \quad (A7)$$

Here,  $f_\alpha$  is the factor dependent on the instantaneous  $\alpha$  as

$$f_\alpha = \begin{cases} 1 & -45^\circ < \alpha < 45^\circ, \\ -1 & 135^\circ < \alpha < 225^\circ, \\ \sqrt{2} \cos \alpha & \text{otherwise.} \end{cases} \quad (A8)$$

Moreover,  $f_r$  is the factor due to the location of the wing's pitching axis with respect to the leading edge ( $x_{rot}$ ) as

$$f_r = 1.57 - 1.239 \left( \frac{1}{Rc} \int_0^R x_{rot} dr \right). \quad (A9)$$

Similarly, the force  $F_{rot,2}$  can be predicted by

$$F_{rot,2} = 2.67 \rho \dot{\alpha} |\dot{\alpha}| \int_{LE}^{TE} r x |x| dx, \quad (A10)$$

where  $x$  is the chordwise distance measured from the pitch axis and is positive in the direction towards the trailing edge (TE).

- [1] A. R. Ennos, Inertial and aerodynamic torques on the wings of diptera in flight, *J. Exp. Biol.* **142**, 87 (1989).
- [2] D. Lentink, W. B. Dickson, J. L. Van Leeuwen, and M. H. Dickinson, Leading-edge vortices elevate lift of autorotating plant seeds, *Science* **324**, 1438 (2009).
- [3] J. W. Kruyt, G. F. van Heijst, D. L. Altshuler, and D. Lentink, Power reduction and the radial limit of stall delay in revolving wings of different aspect ratio, *J. R. Soc. Interface* **12**, 20150051 (2015).
- [4] T. Maxworthy, Experiments on the Weis-Fogh mechanism of lift generation by insects in hovering flight. Part 1. Dynamics of the “fling,” *J. Fluid Mech.* **93**, 47 (1979).
- [5] C. P. Ellington, C. van den Berg, A. P. Willmott, and A. L. R. Thomas, Leading-edge vortices in insect flight, *Nature (London)* **384**, 626 (1996).
- [6] M. H. Dickinson, F.-O. Lehmann, and S. P. Sane, Wing rotation and the aerodynamic basis of insect flight, *Science* **284**, 1954 (1999).
- [7] D. Lentink and M. H. Dickinson, Rotational accelerations stabilize leading edge vortices on revolving fly wings, *J. Exp. Biol.* **212**, 2705 (2009).
- [8] S. P. Sane and M. H. Dickinson, The control of flight force by a flapping wing: Lift and drag production, *J. Exp. Biol.* **204**, 2607 (2001).
- [9] D. J. Garmann and M. R. Visbal, A numerical study of hovering wings undergoing revolving or translating motions, in *Proceedings of the 31st AIAA Applied Aerodynamics Conference*, AIAA Paper 2013-3052 (AIAA, San Diego, CA, 2013).
- [10] Q. Wang, J. F. L. Goosen, and F. van Keulen, A predictive quasi-steady model of aerodynamic loads on flapping-wings, *J. Fluid Mech.* **800**, 688 (2016).
- [11] T. Jardin, Coriolis effect and the attachment of the leading edge vortex, *J. Fluid Mech.* **820**, 312 (2017).
- [12] J. D. Eldredge and A. R. Jones, Leading-edge vortices: Mechanics and modeling, *Annu. Rev. Fluid Mech.* **51**, 75 (2019).
- [13] N. H. Werner, J. Wang, H. Dong, A. E. Panah, and B. Cheng, Scaling the vorticity dynamics in the leading-edge vortices of revolving wings with two directional length scales, *Phys. Fluids* **32**, 121903 (2020).
- [14] L. Chen, C. Zhou, N. H. Werner, B. Cheng, and J. Wu, Dual-stage radial-tangential vortex tilting reverses radial vorticity and contributes to leading-edge vortex stability on revolving wings, *J. Fluid Mech.* **963**, A29 (2023).
- [15] J. M. Birch, W. B. Dickson, and M. H. Dickinson, Force production and flow structure of the leading edge vortex on flapping wings at high and low Reynolds numbers, *J. Exp. Biol.* **207**, 1063 (2004).
- [16] L. Chen, C. Zhou, and J. Wu, The role of effective angle of attack in hovering pitching-flapping-perturbed revolving wings at low Reynolds number, *Phys. Fluids* **32**, 011906 (2020).
- [17] K. Sum Wu, J. Nowak, and K. S. Breuer, Scaling of the performance of insect-inspired passive-pitching flapping wings, *J. R. Soc. Interface* **16**, 20190609 (2019).
- [18] W. J. McCroskey, Unsteady airfoils, *Annu. Rev. Fluid Mech.* **14**, 285 (1982).
- [19] J. M. Walker, H. E. Helin, and J. H. Strickland, An experimental investigation of an airfoil undergoing large-amplitude pitching motions, *AIAA J.* **23**, 1141 (1985).
- [20] M. Acharya and M. H. Metwally, Unsteady pressure field and vorticity production over a pitching airfoil, *AIAA J.* **30**, 403 (1992).
- [21] M. V. Ol, J. D. Eldredge, Y. Lian, D. J. Garmann, and A. Altman, Résumé of the AIAA FDTC Low Reynolds Number Discussion Group’s Canonical Cases, in *Proceedings of the 48th AIAA Aerospace Sciences Meeting* (American Institute of Aeronautics and Astronautics, 2010), pp. 1–18.
- [22] T. C. Corke and F. O. Thomas, Dynamic stall in pitching airfoils: Aerodynamic damping and compressibility effects, *Annu. Rev. Fluid Mech.* **47**, 479 (2015).
- [23] S. S. Bhat and R. N. Govardhan, Stall flutter of NACA 0012 airfoil at low Reynolds numbers, *J. Fluids Struct.* **41**, 166 (2013).
- [24] K. Menon and R. Mittal, Flow physics and dynamics of flow-induced pitch oscillations of an airfoil, *J. Fluid Mech.* **877**, 582 (2019).
- [25] L. Chen, J. Wu, C. Zhou, S.-J. Hsu, and B. Cheng, Unsteady aerodynamics of a pitching-flapping-perturbed revolving wing at low Reynolds number, *Phys. Fluids* **30**, 051903 (2018).

- [26] L. Chen, Y. Zhang, C. Zhou, and J. Wu, Vorticity dynamics of fully developed leading-edge vortices on revolving wings undergoing pitch-up maneuvers, *Phys. Fluids* **35**, 031904 (2023).
- [27] Y. J. Lee, K. B. Lua, T. T. Lim, and K. S. Yeo, A quasi-steady aerodynamic model for flapping flight with improved adaptability, *Bioinspir. Biomimet.* **11**, 036005 (2016).
- [28] F. Karakas and I. Fenercioglu, Effect of side-walls on flapping-wing power-generation: An experimental study, *J. Appl. Fluid Mech.* **9**, 2769 (2016).
- [29] S. Mazharmanesh, J. Stallard, A. Medina, A. Fisher, N. Ando, F.-B. Tian, J. Young, and S. Ravi, Effects of uniform vertical inflow perturbations on the performance of flapping wings, *R. Soc. Open Sci.* **8**, 210471 (2021).
- [30] S. S. Bhat, J. Zhao, J. Sheridan, K. Hourigan, and M. C. Thompson, The leading-edge vortex on a rotating wing changes markedly beyond a certain central body size, *R. Soc. Open Sci.* **5**, 172197 (2018).
- [31] R. R. Harbig, J. Sheridan, and M. C. Thompson, Reynolds number and aspect ratio effects on the leading-edge vortex for rotating insect wing planforms, *J. Fluid Mech.* **717**, 166 (2013).
- [32] S. S. Bhat, J. Zhao, J. Sheridan, K. Hourigan, and M. C. Thompson, Aspect ratio studies on insect wings, *Phys. Fluids* **31**, 121301 (2019).
- [33] S. P. Sane and M. H. Dickinson, The aerodynamic effects of wing rotation and a revised quasi-steady model of flapping flight, *J. Exp. Biol.* **205**, 1087 (2002).
- [34] Q. T. Truong, Q. V. Nguyen, V. T. Truong, H. C. Park, D. Y. Byun, and N. S. Goo, A modified blade element theory for estimation of forces generated by a beetle-mimicking flapping wing system, *Bioinspir. Biomimet.* **6**, 036008 (2011).
- [35] J.-S. Han, J.-K. Kim, J. W. Chang, and J. H. Han, An improved quasi-steady aerodynamic model for insect wings that considers movement of the center of pressure, *Bioinspir. Biomimet.* **10**, 046014 (2015).
- [36] S. S. Bhat, J. Zhao, J. Sheridan, K. Hourigan, and M. C. Thompson, Uncoupling the effects of aspect ratio, Reynolds number and Rossby number on a rotating insect-wing planform, *J. Fluid Mech.* **859**, 921 (2019).
- [37] Z. R. Carr, A. C. DeVoria, and M. J. Ringuette, Aspect-ratio effects on rotating wings: Circulation and forces, *J. Fluid Mech.* **767**, 497 (2015).
- [38] L. Chen, J. Wu, and B. Cheng, Leading-edge vortex formation and transient lift generation on a revolving wing at low Reynolds number, *Aerosp. Sci. Technol.* **97**, 105589 (2020).
- [39] M. R. A. Nabawy and W. J. Crowther, The role of the leading edge vortex in lift augmentation of steadily revolving wings: A change in perspective, *J. R. Soc. Interface* **14**, 20170159 (2017).
- [40] X. Guo, D. Chen, and H. Liu, Does a revolving wing stall at low Reynolds numbers? *J. Biomech. Sci. Eng.* **10**, 15-00588 (2015).
- [41] K. Menon and R. Mittal, Aerodynamic characteristics of canonical airfoils at low Reynolds numbers, *AIAA J.* **58**, 977 (2020).
- [42] P. Broadley, M. R. Nabawy, M. K. Quinn, and W. J. Crowther, Wing planform effects on the aerodynamic performance of insect-like revolving wings, in *Proceedings of the AIAA Aviation 2020 Forum*, AIAA paper 2020-2667 (AIAA, Reston, VA, 2020).
- [43] L. E. Ericsson and J. P. Reding, Fluid mechanics of dynamic stall part I: Unsteady flow concepts, *J. Fluids Struct.* **2**, 1 (1988).
- [44] K. Mulleners and M. Raffel, Dynamic stall development, *Exp. Fluids* **54**, 1469 (2013).
- [45] M. R. Visbal and D. J. Garmann, Analysis of dynamic stall on a pitching airfoil using high-fidelity large-eddy simulations, *AIAA J.* **56**, 46 (2018).
- [46] J. C. R. Hunt, A. A. Wray, and P. Moin, Eddies, streams, and convergence zones in turbulent flows, in *Center for Turbulence Research Report CTR-S88* (CTR, Stanford, CA, 1988), pp. 193–208.